Lawrence Berkeley National Laboratory
LBL Publications

Title
Capturing Nucleation at 4D Atomic Resolution

Permalink
https://escholarship.org/uc/item/7zj48047

Authors
Zhou, Jihan
Yang, Yongsoo
Yang, Yao
et al.

Publication Date
2018-07-27

Peer reviewed

Capturing nucleation at 4D atomic resolution

Jihan Zhou[1*], Yongsoo Yang[1*], Yao Yang[1], Dennis S. Kim[1], Andrew Yuan[1], Xuezeng Tian[1], Colin Ophus[2], Fan Sun[3], Andreas K. Schmid[2], Michael Nathanson[4], Hendrik Heinz[4], Qi An[5], Hao Zeng[3], Peter Ercius[2] & Jianwei Miao[1**]

[1]Department of Physics & Astronomy and California NanoSystems Institute, University of California, Los Angeles, CA 90095, USA. [2]National Center for Electron Microscopy, Molecular Foundry, Lawrence Berkeley National Laboratory, Berkeley, CA 94720, USA. [3]Department of Physics, University at Buffalo, the State University of New York, Buffalo, NY 14260, USA. [4]Department of Chemical and Biological Engineering, University of Colorado at Boulder, Boulder, CO 80309, USA. [5]Chemical and Materials Engineering, University of Nevada, Reno, NV 89557-0388, USA.

[*]These authors contributed equally to this work.

[**]Correspondence and requests for materials should be addressed to J.M. (miao@physics.ucla.edu).

Nucleation plays a critical role in many physical and biological phenomena ranging from crystallization, melting and evaporation to the formation of clouds and the initiation of neurodegenerative diseases. However, nucleation is a challenging process to study especially in the early stage when several atoms/molecules start to form a new phase from its parent phase. Here, we advance atomic electron tomography to study early stage nucleation at 4D atomic resolution. Using FePt nanoparticles as a model system, we reveal that early stage nuclei are irregularly shaped, each has a core of a maximum order parameter, and an order parameter gradient points from the core to the boundary of the nucleus. We capture the structure and dynamics of the same nuclei undergoing growth,

fluctuation, dissolution, merging and/or division, which are regulated by the distribution of the order parameter and its gradient. These experimental results differ from classical nucleation theory (CNT) and to explain them we propose an order parameter gradient model, which is more general and thermodynamically more favourable than CNT. We further corroborate this model using molecular dynamics simulations of heterogeneous and homogeneous nucleation in the liquid-solid phase transition of Pt. We anticipate that the order parameter gradient model is applicable to different kinds of nucleation processes and our experimental method opens the door to study the structure and dynamics of materials with 4D atomic resolution.

Nucleation is a ubiquitous phenomenon in many scientific disciplines[1-3]. To study the nucleation mechanism, an ideal method would be to determine the 3D atomic or molecular structure of newly formed nuclei and monitor their dynamics. Although crystallography has long been used to determine the 3D atomic structure of molecules[4], it cannot be applied to study nucleation due to its requirement of a global average of many identical unit cells, whereas nuclei form locally and irregularly. Over the years, a number of experimental and computational methods have been implemented to investigate nucleation processes, such as x-ray scattering[5,6], electron microscopy[7-10], scanning probe microscopy[11], atom probe tomography[12], video and confocal microscopy of hard-sphere colloids[13-15], molecular dynamics (MD) and Monte Carlo simulations[16-20], and others[1,21]. Despite all these developments, however, it remains unachievable to directly determine the 3D atomic structure of early stage nuclei and monitor their evolution.

On the theoretical side, CNT has been the most widely used model to describe nucleation processes[1-3,22]. While CNT can explain many nucleation phenomena, in some cases its predicted nucleation rates can differ from the measured values by several orders of magnitude[1,23,24]. To alleviate these inconsistencies, non-classical nucleation theories have been proposed, including the density functional theory[25,26,1], the diffuse interface theory[27,28,1] and the dynamical nucleation theory[29]. In recent years, a two-step nucleation model has gained attraction, driven by both computational and experimental results[16,23,24,30,31]. But, a more recent study of the crystallization of the protein glucose isomerase suggested that the nucleation pathway is in accordance with CNT and diverges from the two-step model[10]. The inconsistencies and difficulties associated with nucleation theories can be partially attributed to two reasons. First, nucleation is such a widespread phenomenon existing in many physical, chemical and biological processes[1-3]. Second, a direct experimental method to determine the 3D atomic structure of nuclei and monitor their dynamics is still lacking.

Here, we implement atomic electron tomography (AET)[32], a method capable of determining the 3D atomic coordinates of materials without the assumption of crystallinity[33,34], to study early stage nucleation dynamics. By annealing and quenching the same FePt nanoparticles at multiple times, we probe the evolution of the 4D atomic structure of early stage nuclei. We observe that nucleation starts on the surface of the nanoparticles (i.e. heterogeneous nucleation) and we capture the same nuclei undergoing growth, fluctuation, dissolution, merging and/or division. We discover that nucleation dynamics are regulated by the order parameter and its gradient in the nuclei. To explain these experimental observations, we propose an order parameter gradient (OPG) nucleation model of which CNT represents a special case. We show that the

OPG model has lower free energy barriers to nucleation than that of CNT, indicating that the former is thermodynamically more favourable than the latter. We further corroborate the OPG model by performing MD simulations of both homogeneous and heterogeneous nucleation in the liquid-solid phase transition of Pt.

Capturing 4D atomic motion with AET

AET has been used to reveal the 3D atomic structure of dislocations, stacking faults, grain boundaries, chemical order/disorder and point defects, and determine the atomic displacement and strain tensor with high precision[32-39]. But all of these studies were of static structures. To probe the 4D atomic structure of early stage nucleation, we have tracked the same nuclei at different annealing times and applied AET to determine their 3D atomic positions at each time (Methods). We used FePt nanoparticles as a model system because binary alloys have been widely used to study phase transitions[2] and the precise control of the ordered face-centred tetragonal ($L1_0$) phase of FePt during growth and annealing is important for the development of next generation magnetic recording media[40,41]. To validate the experimental method, we first performed a consistency check experiment of FePt nanoparticles undergoing phase transitions. We annealed the nanoparticles at 520°C for 9 minutes in vacuum and acquired two independent, sequential tilt series of an FePt nanoparticle (termed particle 1) using an annular dark-field scanning transmission electron microscope[42,43] (Methods and Supplementary Table 1). After reconstructing the two data sets using a GENeralized Fourier Iterative REconstruction algorithm (GENFIRE)[34,44], we located and identified the individual Fe and Pt atoms without the assumption of crystallinity (Methods). Supplementary Figs. 1a-f show the 3D atomic models obtained from the two independent data sets of the same nanoparticle. By comparing their 3D atomic coordinates, we confirmed that 95.4%

of atoms are consistent between the two models and the precision of our 3D atomic structure determination method is 26 pm (Supplementary Fig. 1g).

Next, we trapped the same FePt nanoparticles at different annealing times and acquired a tilt series at each time (Methods). By applying the same reconstruction, atom tracing, atom identification and refinement procedures, we obtained a 3D atomic model for each tilt series. Figures 1a-c show the atomic models of the same nanoparticle (named particle 2) with an accumulated annealing time of 9, 16 and 26 minutes, respectively, where Fe atoms are in red and Pt atoms in blue. We observed that the total number of the atoms in the nanoparticle was slightly changed at the three annealing times (Supplementary Table 1). This was caused by the diffusion of individual atom between the substrate and the nanoparticle during the annealing process, which was confirmed by an energy-dispersive x-ray spectroscopy experiment (Supplementary Fig. 2a-d). The overall 3D shape was similar for the nanoparticle annealed at 9 and 16 minutes, but changed from 16 to 26 minutes. A fraction of the surface and sub-surface atoms were re-arranged during the annealing process, but the Pt-rich core of the nanoparticle remained the same (Figs. 1d-f), which is evident by comparing the same internal atomic layers along the [010] direction (Figs. 1g-i). These experimental observations can be explained by vacancy-mediated atomic diffusion as it is energetically more favourable to create vacancies on the surface and sub-surface than in the core of the nanoparticle during annealing[2]. Supplementary Fig. 2e-j shows the 3D atomic models of another FePt nanoparticle (named particle 3) with an accumulated annealing time of 9 and 16 minutes, exhibiting similar results to Fig. 1.

Revealing the heterogeneous nucleation sites

The annealed FePt nanoparticles consist of three phases: an $L1_0$ phase, a chemically disordered face-centred cubic (fcc) structure (A1 phase) and a chemically ordered fcc ($L1_2$) phase. We quantified these phases using the short-range order parameter[34] (for simplicity we term it the order parameter throughout this article). Based on the order parameter, we identified nuclei with the $L1_0$, Fe-rich A1, Pt-rich A1, Fe-rich $L1_2$ and Pt-rich $L1_2$ phases in these nanoparticles (Methods), in which a nucleus is defined to have a minimum of 13 atoms. As the $L1_0$ phase nuclei are more abundant in the nanoparticles and this phase is also more technologically important[40,41], we focused on the analysis of the $L1_0$ phase nuclei in this work. Careful examination of all the nuclei indicates that each nucleus has a core of a maximum order parameter. To locate the nucleation sites, we searched for the cores of all the $L1_0$ phase nuclei inside the nanoparticles. The distribution of the nucleation sites in particle 1 is in agreement (Supplementary Fig. 3a-c). Figure 2a-d and Supplementary Fig. 3d-f show the evolution of the nucleation sites as a function of the annealing time in particles 2 and 3, respectively. If the core of a nucleus is within one unit cell distance (3.87 Å) from the surface, we define it as a surface site. Otherwise, it is defined as a sub-surface site. Most nucleation sites in particles 2 and 3 are located on the facets, edges or corners, where the <100> and <111> facets are shown in magenta and green colour, respectively. Compared to particles 2 and 3, particle 1 has more nucleation sites at the sub-surface, because many nuclei in particle 1 are relatively large and their cores are more than one unit cell distance from the surface. All our observations confirm that the nucleation is heterogeneous, which is energetically more favourable than homogeneous nucleation[1-3].

Capturing nucleation dynamics at 4D atomic resolution

To probe early stage nucleation dynamics, we identified the common nuclei among the different annealing time data. Using the criterion of a common nucleus consisting of at least 50% overlapping atoms between two consecutive annealing times, we located 33 and 25 common nuclei in particles 2 and 3, respectively (Methods). As each atom is associated with an order parameter, we define the effective number of atoms by summing up all the order parameters in each nucleus. We found that the order parameter of the nucleus core (α_0) is correlated with the effective number of atoms. Larger nuclei tend to have cores with higher order parameters (Supplementary Fig. 3g). Based on the effective number of atoms, we divided the common nuclei into three groups: growing, fluctuating and dissolving nuclei (Methods). Figure 3 shows five growing, fluctuating and dissolving nuclei in particle 2, where each nucleus is represented by an atomic model and a 3D contour map with an order parameter equal to 0.7 (red), 0.5 (purple) and 0.3 (light blue). There are 14 growing, 14 fluctuating and 5 dissolving nuclei in particle 2 (Fig. 3, Supplementary Figs. 4, 5, and 6a-d), while there are 16 growing and 9 dissolving nuclei in particle 3. Among these common nuclei, we also observed merging and dividing nuclei, shown in Fig. 3g-i, Supplementary Figs. 4b-d and 5e.

In addition to the effective number of atoms, we found that the OPG also plays an important role in nucleation dynamics, which points from the core of each nucleus to its boundary. Figure 4a-c show the order parameter distribution of a growing nucleus in particle 2 (Fig. 3a-c) along the [110], [111] directions and with radial average, respectively, where the order parameter increases with the increment of the annealing time. Figure 4d-f shows the 3D OPG distribution of the same nucleus at three different annealing times. As the nucleus grows, the OPG spreads out further along the radial direction. These observations are corroborated by the analysis of other growing,

fluctuating and dissolving nuclei (Supplementary Fig. 7). To perform a quantitative analysis, we summed up all the OPG inside each nucleus, which we term the effective surface area of the nucleus as it has the same dimension as area. Figure 2e shows a plot of the effective surface area vs. the effective number of atoms for all the nuclei in particles 2 and 3. The dissolving nuclei are clustered near the lower left corner of the plot, but both small and large nuclei can fluctuate as a function of the time.

The order parameter gradient nucleation model

Our experimental study of early stage nucleation reveals four observations that cannot be explained by CNT[1,2,22]. First, early stage nuclei are anisotropic, which were characterized using sphericity[45], a measure of how closely the shape of a 3D object approaches a perfect sphere. Supplementary Fig. 3h shows the sphericity of the nuclei as a function of the effective number of atoms, indicating that the majority of the nuclei have a sphericity between 0.5 and 0.9 (with 1.0 as a perfect sphere). Second, each nucleus has a core of a maximum order parameter and the OPG points from the core to the boundary (Fig. 4d-f and Supplementary Fig. 3g). Third, the interface between a nucleus and its parent phase is not sharp but smooth, which is regulated by the order parameter and its gradient (Fig. 4 and Supplementary Fig. 7). Fourth, fluctuations were observed for both small and large nuclei, indicating that there is not a single critical radius as defined in CNT[1,2,22] (Fig. 3d-l and Supplementary Fig. 5). To account for these experimental results, we propose an OPG nucleation model

$$\Delta G = -\Delta g \int \alpha(\vec{r}) \, dV + \gamma \int |\vec{\nabla} \alpha(\vec{r})| \, dV , \qquad (1)$$

where ΔG is the total free energy change, Δg the free energy change per unit volume, $\alpha(\vec{r})$ the order parameter between 0 and 1, and γ the interfacial tension of a sharp interface between a nucleation phase and its parent phase. Although an isotropic γ is

assumed here, an anisotropic interfacial tension can in principle be incorporated into the model. Equation (1) is for homogeneous nucleation and for heterogeneous nucleation it has to be multiplied by a shape factor[1,2]. The first term in equation (1) stands for the volume energy difference of a nucleus. The second term represents the effective interfacial energy of the nucleus, which can be derived by first dividing the nucleus into many very small volumes and then summing up the interfacial energy for all the volumes (Supplementary Fig. 6e and Methods).

The OPG model reduces to CNT when the order parameter is given by

$$\alpha(r) = \begin{cases} 1 & r \leq R \\ 0 & r > R \end{cases}, \qquad (2)$$

where R is the radius of a spherical nucleus. Substituting equation (2) into equation (1), we obtain the total free energy change in CNT[1,2,22]

$$\Delta G = -\frac{4\pi R^3}{3}\Delta g + 4\pi R^2 \gamma . \qquad (3)$$

To provide a better physical understanding of the OPG model, we applied equation (1) to three specific cases with $\alpha(r)$ linearly or parabolically decreasing with the radial distance (Supplementary Fig. 6f and Methods). Our analysis indicates that unlike CNT, the critical radius and free energy barriers to nucleation of the OPG model change as a function of $\alpha(r)$. We have also mathematically proved that if $\alpha(r)$ monotonically decreases as the radial distance, the OPG model always has lower free energy barriers than CNT for both homogeneous and heterogeneous nucleation (Methods).

To apply the OPG model to our experimental data, we fit the order parameter distribution of each nucleus using a generalized Gaussian distribution, which can represent a nucleus core with a smoothly varying boundary,

$$\alpha(r) = \alpha_0 e^{(-r/\lambda)^\beta} , \qquad (4)$$

where α_0, λ and β are the fitting parameters with α_0 representing the order parameter of the nucleus core. Figure 4a-c and Supplementary Fig. 7 show the fitting of equation (4) to the measured order parameter of several representative nuclei, indicating equation (4) (solid curves) is in good agreement with the experimental measurements (dots). According to equation (1), with every change of the order parameter and its gradient in a nucleus, the critical radius and the free energy barrier are altered accordingly, creating a metastable state of the nucleus. Our experimental results indicate that nuclei have various distributions of the order parameter and the gradient (Fig. 4 and Supplementary Fig. 7), resulting in different metastable states. When the difference between two order parameter distributions is small, the gap of the corresponding free energy barriers is narrow, which facilitates the fluctuation of the nucleus between the two metastable states. Numerous such fluctuating nuclei were observed in our experimental data (Fig. 3d-l and Supplementary Fig. 5).

Corroborating the OPG nucleation model with MD simulations

To further validate the OPG model, we performed MD simulations of both heterogeneous and homogeneous nucleation in a liquid-solid phase transition. The simulations were carried out using the large-scale atomic/molecular massively parallel simulator (LAMMPS)[46]. To enable cross-validation of the results, for heterogeneous nucleation we applied both the embedded-atom method potential[47] and the interface force field[48] to simulate two Pt liquid nanodroplets above the melting temperature (Methods). We then lowered the temperature to investigate early stage nucleation during a liquid-solid phase transition. We normalized the average local bond order parameter to analyse the nuclei[49] (Methods). We found that most nuclei are located on or near the surface of the two nanoparticles and every nucleus has a core of a maximum order

parameter. Using the same criterion as the experimental data, we identified the common nuclei among different times and observed nucleation dynamics including growth, fluctuation, and dissolution. Figure 5a-d and Supplementary Fig. 8a-d show four representative growing, fluctuating and dissolving nuclei for the embedded-atom method and the interface force field, respectively, where merging and dividing nuclei were also observed. The order parameter distributions as the radial distance of these nuclei are shown in Fig. 5e-h and Supplementary Fig. 8e-h, indicating that nucleation dynamics is regulated by the distribution of the order parameter and its gradient. For homogeneous nucleation, we used the embedded-atom method potential[47] with periodic boundary condition to simulate a bulk Pt system undergoing a liquid-solid phase transition (Methods). Supplementary Fig. 9 shows four representative growing, fluctuating and dissolving nuclei and their corresponding order parameter distributions as the radial distance. All the MD simulation results of heterogeneous and homogeneous nucleation are consistent with our experimental observations and further validate the OPG model.

Discussion

By trapping the same nuclei at different annealing times, we applied AET to capture the structure and dynamics of the nuclei at 4D atomic resolution. We found that early stage nuclei are nonspherical and every nucleus has a core of a maximum order parameter, creating an OPG pointing from the core to the boundary. We also monitored the same nuclei undergoing growth, fluctuation, dissolution, merging and/or division. To explain these experimental observations, we proposed an OPG nucleation model, which was further corroborated by MD simulations. There are several important implications of this work. First, the OPG model generalizes CNT and only reduces to CNT when the

order parameter function is represented by equation (2). Mathematically, it has been shown that the OPG model is thermodynamically more favourable than CNT (Methods), suggesting that using different order parameters, the OPG model could be applied to other types of nucleation processes. Second, in early stage nucleation, there is a clear difference between OPG and CNT. With the growth of a nucleus, its core becomes larger and the interface between the core and the boundary is narrower. This results in the volume energy difference term dominating over the effective interfacial energy term in equation (1), reducing the difference between OPG and CNT. Third, the OPG model solves an inconsistency problem in CNT[1,22]. For a single molecule, the first term in equation (3) is 0, and the second term is larger than 0, resulting in $\Delta G > 0$. But the OPG model resolves this inconsistency as both terms in equation (1) is 0 for a single molecule.

Fourth, according to CNT[1,2,22], the nucleation rate is proportional to $e^{-\frac{\Delta G^*}{K_B T}}$, where ΔG^* is the free energy barrier to nucleation, K_B the Boltzmann constant and T the temperature. But based on our experimental results and the OPG model, the distribution of the order parameter and its gradient of a nucleus can vary as a function of time and each distribution produces a different critical radius and free energy barrier (i.e. a metastable state). Our experimental and MD results show that early stage nuclei can fluctuate between these metastable states. This may explain some of the discrepancies between experimentally measured nucleation rates and those predicted by CNT[1,23,24]. However, here we focused on the experimental study of nucleation dynamics as a function of time. To fully understand the nucleation rate, additional experiments are needed to investigate nucleation dynamics as a function of temperature with 4D atomic resolution. Fifth, our experimental results on the early stage nucleation of the L1$_0$ FePt

phase can expand our understanding of the critical conditions and requirements to make superior magnetic recording media and catalysts based on binary alloys[40,41,50]. Finally, all the seven experimental atomic models with 3D coordinates reported here will be deposited in the Materials Data Bank, a database to be launched in 2018 to serve the physical science community, which is analogous to the Protein Data Bank for the biological and life science communities. These experimentally measured coordinates can be used as direct input for density functional theory calculations and MD simulations of material properties[34], which is anticipated to open a new window to study the structure-property relationships of materials with 4D atomic resolution.

References

1. Kelton, K. F. & Greer, A. L. *Nucleation in Condensed Matter: Applications in Materials and Biology*. (Pergamon, 2010).
2. Porter, D. A., Easterling, K. E. & Sherif, M. Y. *Phase transformations in metals and alloys*. (CRC Press, 2009).
3. Kashchiev, D. *Nucleation: Basic Theory with Applications*. (Butterworth-Heinemann, 2000).
4. Crystallography at 100. *Science* **343,** (Special issue), 1091-1116 (2014).
5. Kelton, K. F. *et al.* First X-Ray Scattering Studies on Electrostatically Levitated Metallic Liquids: Demonstrated Influence of Local Icosahedral Order on the Nucleation Barrier. *Phys. Rev. Lett.* **90,** 195504 (2003).
6. Kwon, S. G. *et al.* Heterogeneous nucleation and shape transformation of multicomponent metallic nanostructures. *Nat. Mater.* **14,** 215–223 (2015).
7. Nielsen, M. H., Aloni, S. & De Yoreo, J. J. In situ TEM imaging of CaCO3 nucleation reveals coexistence of direct and indirect pathways. *Science* **345,** 1158–1162 (2014).
8. Smeets, P. J. M., Cho, K. R., Kempen, R. G. E., Sommerdijk, N. A. J. M. & De Yoreo, J. J. Calcium carbonate nucleation driven by ion binding in a biomimetic matrix revealed by in situ electron microscopy. *Nat. Mater.* **14,** 394–399 (2015).
9. Pouget, E. M. *et al.* The Initial Stages of Template-Controlled CaCO3 Formation Revealed by Cryo-TEM. *Science* **323,** 1455–1458 (2009).

10. Van Driessche, A. E. S. *et al.* Molecular nucleation mechanisms and control strategies for crystal polymorph selection. *Nature* **556,** 89–94 (2018).

11. Sleutel, M., Lutsko, J., Van Driessche, A. E. S., Durán-Olivencia, M. A. & Maes, D. Observing classical nucleation theory at work by monitoring phase transitions with molecular precision. *Nat. Commun.* **5,** 5598 (2014).

12. Seidman, D. N. Three-Dimensional Atom-Probe Tomography: Advances and Applications. *Annu. Rev. Mater. Res.* **37,** 127–158 (2007).

13. Auer, S. & Frenkel, D. Prediction of absolute crystal-nucleation rate in hard-sphere colloids. *Nature* **409,** 1020–1023 (2001).

14. Gasser, U. Real-Space Imaging of Nucleation and Growth in Colloidal Crystallization. *Science* **292,** 258–262 (2001).

15. Anderson, V. J. & Lekkerkerker, H. N. W. Insights into phase transition kinetics from colloid science. *Nature* **416,** 811–815 (2002).

16. Wolde, P. R. ten & Frenkel, D. Enhancement of Protein Crystal Nucleation by Critical Density Fluctuations. *Science* **277,** 1975–1978 (1997).

17. Matsumoto, M., Saito, S. & Ohmine, I. Molecular dynamics simulation of the ice nucleation and growth process leading to water freezing. *Nature* **416,** 409–413 (2002).

18. Auer, S. & Frenkel, D. Numerical prediction of absolute crystallization rates in hard-sphere colloids. *J. Chem. Phys.* **120,** 3015–3029 (2004).

19. Russo, J. & Tanaka, H. The microscopic pathway to crystallization in supercooled liquids. *Sci. Rep.* **2,** 505 (2012).

20. Merikanto, J., Zapadinsky, E., Lauri, A. & Vehkamäki, H. Origin of the Failure of Classical Nucleation Theory: Incorrect Description of the Smallest Clusters. *Phys. Rev. Lett.* **98,** 145702 (2007).

21. Gebauer, D., Völkel, A. & Cölfen, H. Stable Prenucleation Calcium Carbonate Clusters. *Science* **322,** 1819–1822 (2008).

22. Vehkamäki, H. *Classical nucleation theory in multicomponent systems.* (Springer, 2006).

23. Vekilov, P. G. Nucleation. *Cryst Growth Des* **10,** 5007–5019 (2010).

24. Karthika, S., Radhakrishnan, T. K. & Kalaichelvi, P. A Review of Classical and Nonclassical Nucleation Theories. *Cryst Growth Des* **16,** 6663–6681 (2016).

25. Cahn, J. W. & Hilliard, J. E. Free Energy of a Nonuniform System. III. Nucleation in a Two-Component Incompressible Fluid. *J. Chem. Phys.* **31,** 688–699 (1959).

26. Oxtoby, D. W. & Evans, R. Nonclassical nucleation theory for the gas–liquid transition. *J. Chem. Phys.* **89,** 7521–7530 (1988).

27. Gránásy, L. Diffuse interface theory of nucleation. *J. Non-Cryst. Solids* **162,** 301–303 (1993).

28. Spaepen, F. Homogeneous nucleation and the temperature dependence of the crystal–melt interfacial tension. in *Solid State Physics* (eds. Ehrenreich, H. & Turnbull, D.) 1–32 (Academic Press, New York, 1994).

29. Schenter, G. K., Kathmann, S. M. & Garrett, B. C. Dynamical Nucleation Theory: A New Molecular Approach to Vapor-Liquid Nucleation. *Phys. Rev. Lett.* **82,** 3484–3487 (1999).

30. Peng, Y. *et al.* Two-step nucleation mechanism in solid–solid phase transitions. *Nat. Mater.* **14,** 101–108 (2015).

31. Savage, J. R. & Dinsmore, A. D. Experimental Evidence for Two-Step Nucleation in Colloidal Crystallization. *Phys. Rev. Lett.* **102,** 198302 (2009).

32. Miao, J., Ercius, P. & Billinge, S. J. L. Atomic electron tomography: 3D structures without crystals. *Science* **353,** aaf2157 (2016).

33. Xu, R. *et al.* Three-dimensional coordinates of individual atoms in materials revealed by electron tomography. *Nat. Mater* **14,** 1099–1103 (2015).

34. Yang, Y. *et al.* Deciphering chemical order/disorder and material properties at the single-atom level. *Nature* **542,** 75–79 (2017).

35. Scott, M. C. *et al.* Electron tomography at 2.4-angstrom resolution. *Nature* **483,** 444–447 (2012).

36. Goris, B. *et al.* Three-Dimensional Elemental Mapping at the Atomic Scale in Bimetallic Nanocrystals. *Nano Lett.* **13,** 4236–4241 (2013).

37. Chen, C.-C. *et al.* Three-dimensional imaging of dislocations in a nanoparticle at atomic resolution. *Nature* **496,** 74–77 (2013).

38. Goris, B. *et al.* Measuring Lattice Strain in Three Dimensions through Electron Microscopy. *Nano Lett.* **15,** 6996–7001 (2015).

39. Haberfehlner, G. *et al.* Formation of bimetallic clusters in superfluid helium nanodroplets analysed by atomic resolution electron tomography. *Nat. Commun.* **6,** 8779 (2015).

40. Sun, S. Monodisperse FePt Nanoparticles and Ferromagnetic FePt Nanocrystal Superlattices. *Science* **287,** 1989–1992 (2000).

41. Ju, G. *et al.* High Density Heat-Assisted Magnetic Recording Media and Advanced Characterization—Progress and Challenges. *IEEE Trans. Magn.* **51,** 3201709 (2015).

42. Pennycook, S. J. & Nellist, P. D. *Scanning Transmission Electron Microscopy: Imaging and Analysis*. (Springer Science & Business Media, 2011).

43. Muller, D. A. Structure and bonding at the atomic scale by scanning transmission electron microscopy. *Nat. Mater.* **8,** 263–270 (2009).

44. Pryor, A. *et al.* GENFIRE: A generalized Fourier iterative reconstruction algorithm for high-resolution 3D imaging. *Sci. Rep.* **7,** 10409 (2017).

45. Wadell, H. Volume, Shape, and Roundness of Quartz Particles. *J. Geol.* **43,** 250–280 (1935).

46. Plimpton, S. Fast Parallel Algorithms for Short-Range Molecular Dynamics. *J. Comput. Phys.* **117,** 1–19 (1995).

47. Zhou, X. W., Johnson, R. A. & Wadley, H. N. G. Misfit-energy-increasing dislocations in vapor-deposited CoFe/NiFe multilayers. *Phys. Rev. B* **69,** 144113 (2004).

48. Heinz, H., Vaia, R. A., Farmer, B. L. & Naik, R. R. Accurate Simulation of Surfaces and Interfaces of Face-Centered Cubic Metals Using 12−6 and 9−6 Lennard-Jones Potentials. *J. Phys. Chem. C* **112,** 17281–17290 (2008).

49. Lechner, W. & Dellago, C. Accurate determination of crystal structures based on averaged local bond order parameters. *J. Chem. Phys.* **129,** 114707 (2008).

50. Paulus, U. A. *et al.* Oxygen Reduction on Carbon-Supported Pt−Ni and Pt−Co Alloy Catalysts. *J. Phys. Chem. B* **106,** 4181–4191 (2002).

Data availability The raw and processed experimental data sets as well as all the Matlab source codes for the image reconstruction and data analysis approaches described in Methods will be freely available at www.physics.ucla.edu/research/imaging/OPG immediately after this work is published. The 3D atomic coordinates of particles 1, 2 and 3 at different annealing times will be deposited in the Materials Data Bank (http://wwmdb.org).

Figures and Figure legends
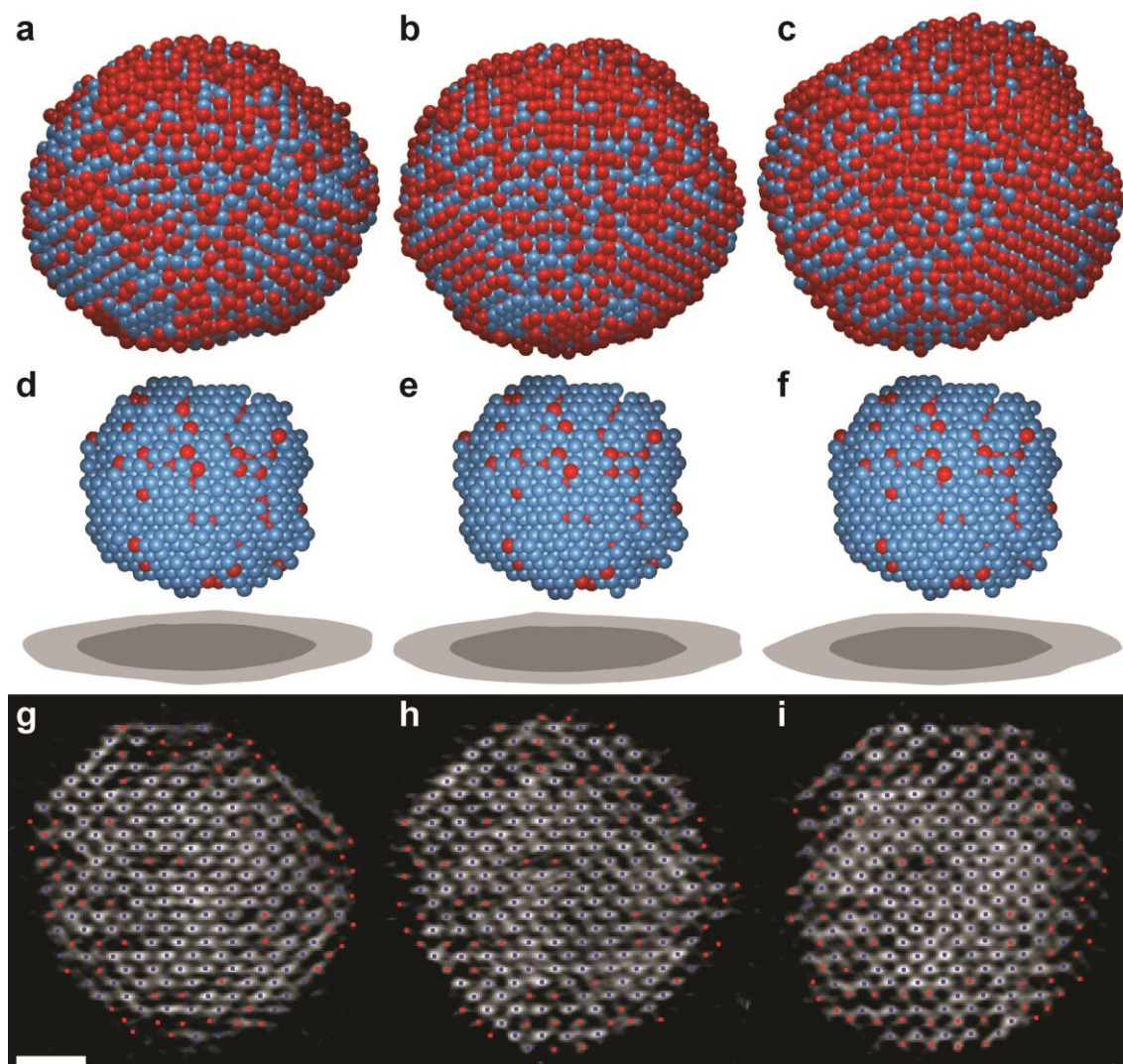
Figure 1 | Capturing 4D atomic motion with AET. **a-c,** 3D atomic models (Fe in red and Pt in blue) of an FePt nanoparticle with an accumulated annealing time of 9, 16 and 26 minutes, respectively, determined by AET. The 3D shape of the nanoparticle was similar from 9 to 16 minutes, but changed from 16 to 26 minutes. **d-f,** The Pt-rich core of the nanoparticle remained the same for the three annealing times. The light and dark grey projections show the whole nanoparticle and the core, respectively. **g-i,** The same internal atomic layer of the nanoparticle along the [010] direction at the three annealing times (Pt in blue and Fe in red), where a fraction of the surface and sub-surface atoms

were re-arranged during the annealing process, but the Pt-rich core of the nanoparticle did not change.
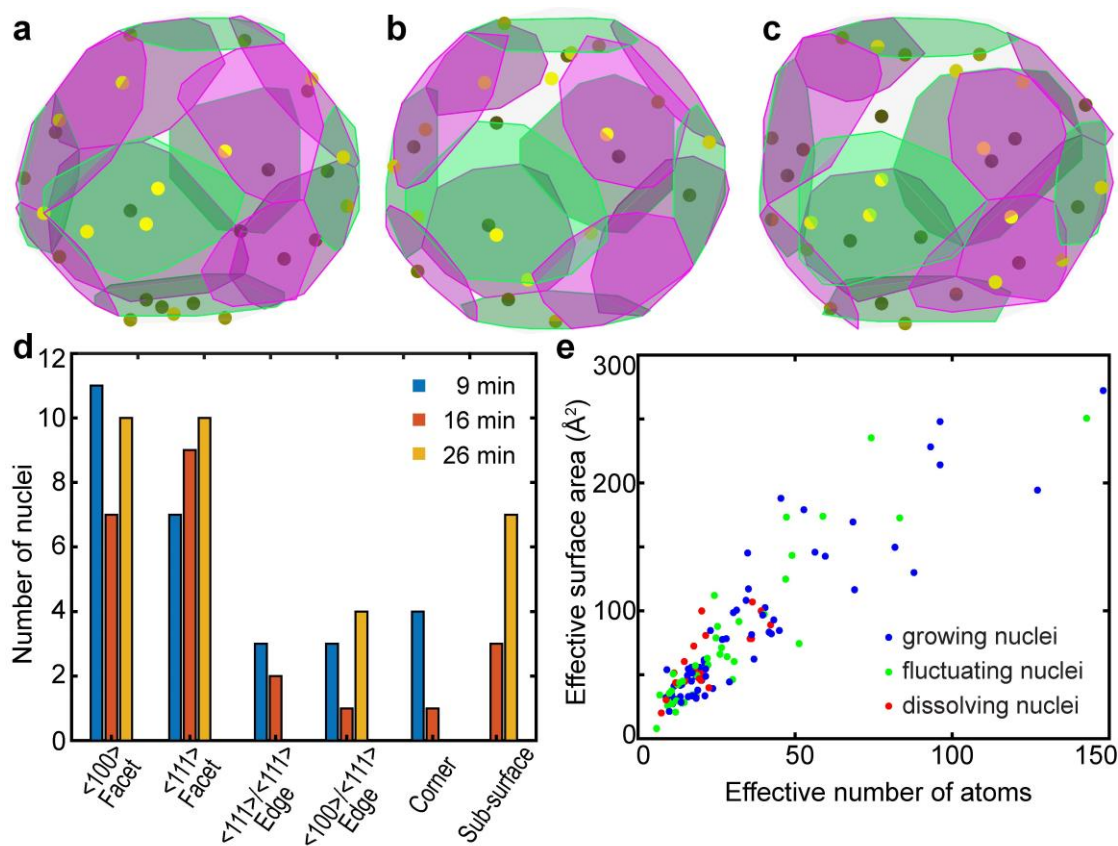
Figure 2 | Revealing the heterogeneous nucleation sites. **a-c**, The distribution of the nucleation sites (circular dots) in particle 2 with an accumulated annealing time of 9, 16 and 26 minutes, respectively, where the lighter coloured dots are closer to the front side and the darker dots are closer to the back side of the nanoparticle. The <100> and <111> facets are in magenta and green, respectively. **d**, The histogram of the nucleation site distribution in particle 2, where most nucleation sites are located on the facets, edges or corners. **e**, A plot of the effective surface area vs. the effective number of atoms for all the nuclei in particles 2 and 3. While the dissolving nuclei are clustered near the lower left corner, both small and large fluctuating nuclei are observed.
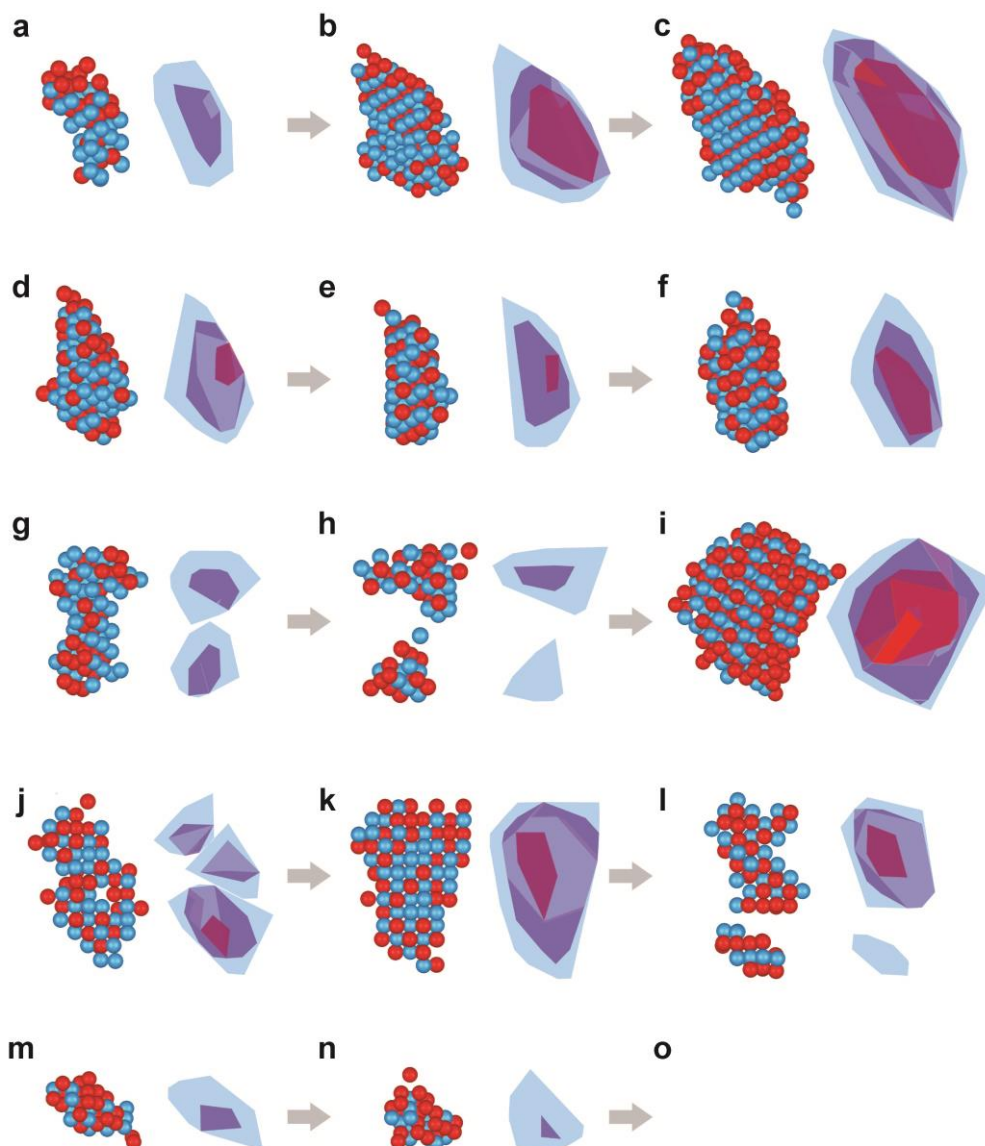
Figure 3 | Experimental observation of the same nuclei undergoing growth, fluctuation, dissolution, merging and/or division at 4D atomic resolution. a-c, A representative growing nucleus with an accumulated annealing time of 9, 16 and 26 minutes, respectively, where the atomic models show Fe (red) and Pt (blue) atoms with an order parameter ≥ 0.3 and the 3D contour maps show the distribution of an order parameter of 0.7 (red), 0.5 (purple) and 0.3 (light blue). **d-l**, Three representative fluctuating nuclei at three annealing times, including merging and dividing nuclei. **m-o**,

A representative dissolving nucleus at three annealing times, which dissolved at 26 minutes (**o**).
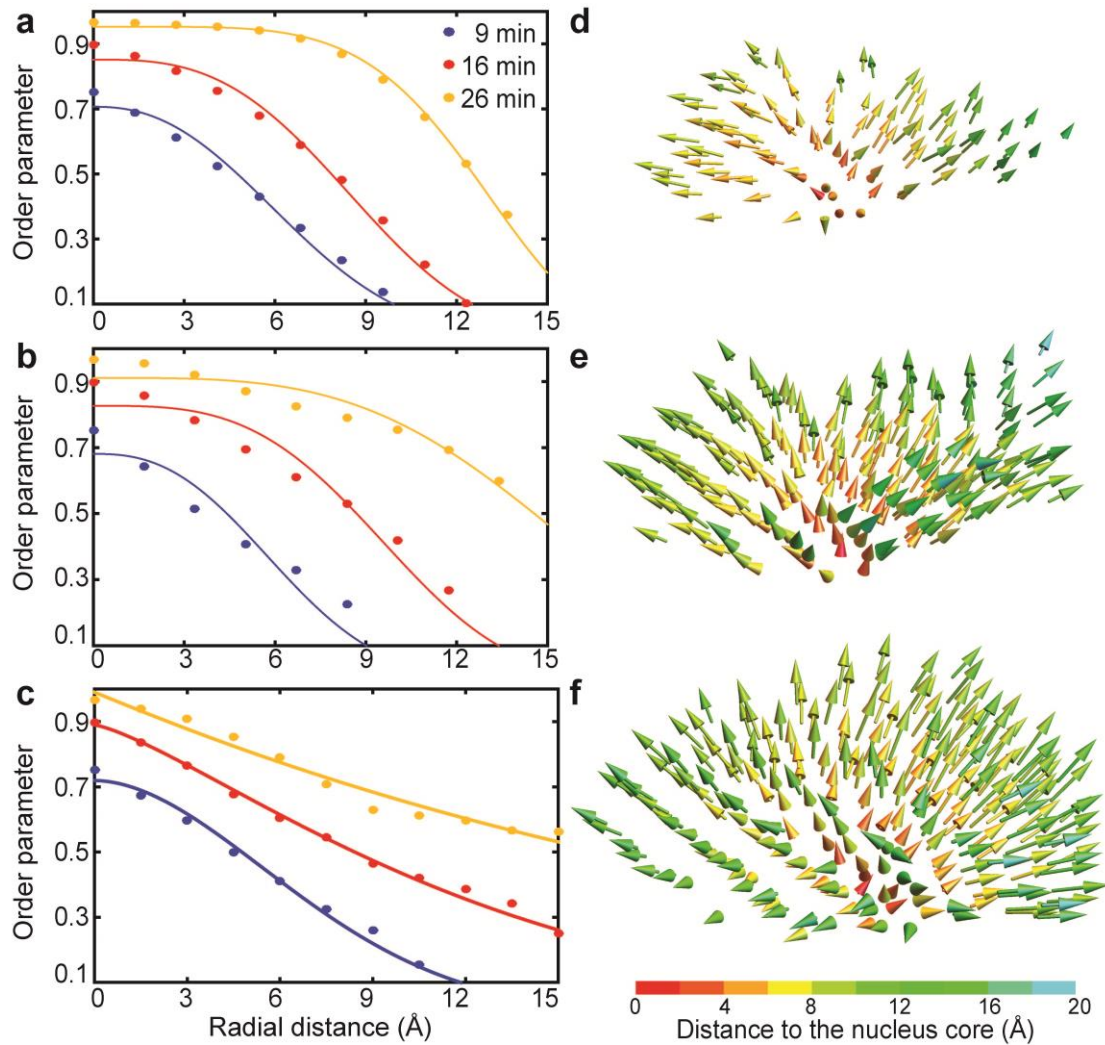
Figure 4 | The 3D distribution of the order parameter and its gradient inside a representative nucleus. **a-c**, The order parameter distribution of a growing nucleus (Fig. 3a-c) along the [110], [111] directions and with radial average, respectively, where the dots represent the experimental data and the curves are the fitted results with equation (4). **d-f**, The 3D OPG distribution of the nucleus at three annealing times, respectively, where the colours represent the distance to the nucleus core. With the growth of the nucleus, the OPG spreads out further along the radial direction.
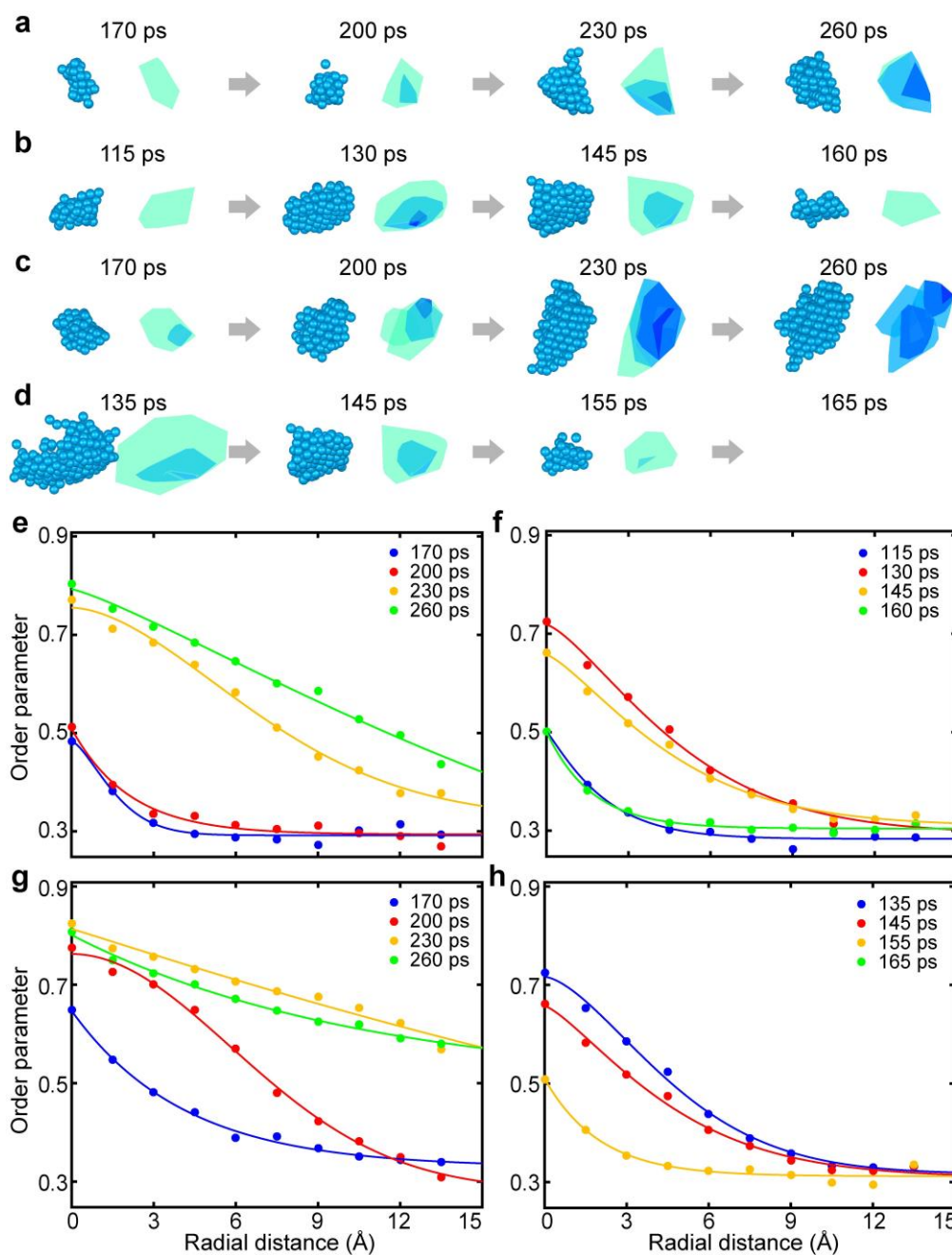
Figure 5 | Nucleation dynamics in the liquid-solid phase transition of a Pt nanoparticle, obtained by MD simulations with the embedded-atom method potential. **a**, A representative growing nucleus, where the atomic models show the Pt atoms with an order parameter ≥ 0.3 and the 3D contour maps show the distribution of an order parameter of 0.7 (dark blue), 0.5 (light blue) and 0.3 (cyan). **b** and **c**, Two representative fluctuating nuclei, where merging and dividing nuclei were observed in

(**c**). **d**, A representative dissolving nucleus, which dissolved at 165 ps. **e-h**, Radial average order parameter distributions of the four nuclei shown in (**a-d**), respectively, where the dots were obtained by time-averaging ten consecutive MD snapshots with 1 ps time intervals and the curves are the fitted results using equation (4) with a constant background. The results indicate that nucleation dynamics are regulated by the distribution of the order parameter.

METHODS

Data acquisition. FePt nanoparticles were synthesized using the procedures published elsewhere[51]. After deposited on to 5-nm-thick silicon nitride membranes, the nanoparticles were annealed at 520 °C for 9 minutes in vacuum. A set of tomographic tilt series were acquired from several FePt nanoparticles using the TEAM 0.5 microscope and the TEAM stage. Images were collected at 200 kV in ADF-STEM mode (Supplementary Table 1). To minimize sample drift, four to five images per angle were measured with 3 μs dwell time. For the consistency check experiment, we took a 2nd set of tomographic tilt series from the same nanoparticles under the identical experimental conditions. For the dynamics study experiment, we took the nanoparticles out of microscope and annealed them at 520 °C for additional 7 minutes. Based on the pattern of the nanoparticle distribution on the substrate, we identified the same nanoparticles and acquired a 2nd set of tomographic tilt series from them. We then annealed the same nanoparticles at 520 °C for additional 10 minutes and acquired a 3rd set of tilt series. We chose three FePt nanoparticles to present in this work. Particle 1 was annealed for 9 minutes and two independent, sequential tilt series were acquired under the same experimental conditions. Particle 2 was annealed with an accumulated time of 9, 16 and 26 minutes and a tilt series was taken at each time. Particle 3 was annealed with an accumulated time of 9 and 16 minutes and a tilt series was acquired at each time. To monitor any potential structural changes induced by the electron beam, we took 0° projection images before, during and after the acquisition of each tilt series and ensured that no noticeable structural changes were observed during the data acquisition for particles 1, 2 and 3. The total electron dose of each tilt series for particles 1, 2 and 3 was estimated to be between 7.6×10^5 e$^-$/Å^2 and 8.5×10^5 e$^-$/Å^2 (Supplementary Table 1), which is 5.6 to 6.3 times lower than that used in ref. 34.

Image post-processing, denoising and GENFIRE reconstructions. The four to five images acquired at each tilt angle were registered using normalized cross correlation[52] and then averaged. Linear stage drift at each tilt angle was estimated and corrected during the image registration. Scan distortion correction was also performed to correct for the imperfections in the calibration of the x- and y- scanning coils[33,34]. The experimental ADF-STEM images have mixed Poisson and Gaussian noise, and a sparse 3D transform-domain collaborative filtering[53] was applied to denoise the average image of each tilt angle.

These post-processing and denoising methods have shown their robustness throughout other experimental data and multislice simulations[33,34].

After background subtraction and alignment, each tilt series was reconstructed using the GENFIRE algorithm[34,44]. From the initial 3D reconstruction, we applied the angular refinement routine implemented in GENFIRE to automatically correct the angular errors due to sample holder rotation and/or stage instability. After the automatic angular refinement, we manually applied additional angular correction and spatial alignment to minimize the distortions of Fourier space peak distributions and reduce the errors between the measured and calculated projections. After no further improvement can be made, we performed the final reconstruction of each tilt series using GENFIRE with the parameters shown in Supplementary Table 1.

Determination of 3D atomic coordinates and species. The 3D atomic coordinates and species of the nanoparticles were identified from the 3D reconstructions using the following procedure.

i) To enhance the tracing accuracy, we upsampled each 3D reconstruction by a factor of 3 using spline interpolation. All the local maxima were identified from the upsampled reconstruction.

ii) We implemented 3D polynomial fitting to localize the peak positions in each reconstruction, which generalizes a 2D method developed in particle tracking[54]. Starting from the highest-intensity local maximum peak, we cropped a $\sim 1.0 \times 1.0 \times 1.0$ Å^3 ($9 \times 9 \times 9$ voxel) volume with the selected local peak as the centre. We fit the volume with a 3D fourth-order polynomial function described elsewhere[54]. If a fitted peak position satisfied with a minimum distance constraint of 2 Å (i.e. the distance between two neighbouring atoms $\geq$ 2 Å), we listed it as a potential atom position. According to our multislice simulations, the 3D polynomial fitting method is more accurate than 3D Gaussian fitting that has been used before[33,34].

iii) By applying the 3D polynomial fitting to all the identified local maxima, we obtained a list of potential atom positions. These positions were manually checked to correct for unidentified or misidentified atoms due to fitting failure or large chunk of connected intensity blobs from multiple atoms.

iv) We classified all the potential atoms into three different categories (non-atoms, potential Fe or Pt atoms) by applying an unbiased atom classification method described elsewhere[34]. With this classification procedure, we obtained an initial atomic model with 3D atomic coordinates and species from each 3D reconstruction.

v) Due to the missing wedge and experimental noise, there is local intensity variation in each 3D reconstruction. To further improve the atom classification accuracy, we performed local re-classification of the Fe and Pt atoms. For each atom in the initial atomic model, we drew a sphere with the atom as the centre and a radius of 6.76 Å. All the Fe and Pt atoms within the sphere were summed up to obtain an average Fe and Pt atom. The intensity distribution of the centre atom was compared with that of the average Fe and Pt atom. If the centre atom was closer to the average Fe than to the average Pt atom, it was assigned as an Fe atom, and vice versa. We iterated this process for all the atoms until the re-classification procedure was converged. Note that this process did not converge if the radius of the sphere was too small, and it became less effective if the radius was too large. By testing different radii, we found an optimal radius of 6.76 Å for this re-classification procedure.

Refinement of 3D atomic coordinates and species. We compared two atomic models of the same nanoparticle with each other. For particles 1 and 3, the two atomic models obtained from two experimental tilt series were compared. For particle 2, the 9-minute and 16-minute atomic models, and then the 16-minute and 26-minute atomic models were compared, respectively. We identified pairs of atoms (i.e. one atom from each model to form a pair), whose distance is within the radius of the Fe atom (1.4 Å). While the majority of the atom pairs have the same atomic species, there are a small percentage of atom pairs with different species. We developed the following atom flipping procedure to re-examine the atomic species of the small percentage of atom pairs.

i) An atom was randomly selected from the small percentage of atom pairs with different species. The projection intensities were calculated for all the tilt angles by flipping the selected atom (Fe to Pt or Pt to Fe), and the error between the calculated and measured projections was estimated. As flipping a single atom only affects a small local region of a projection, we only considered the local region in this process to increase the computational speed.

ii) If the error decreased after flipping, the flipped atomic species was updated in the model, otherwise the model was unchanged.

iii) Steps i) and ii) were repeated for all the small percentage of atom pairs and an updated atomic model was obtained. A global scale factor was calculated to minimize the error between the measured and calculated projections.

iv) Steps i)-iii) were iterated for all the small percentage of atom pairs until there was no change in the atomic species. This atom flipping method successfully converged for all datasets that we studied in this work.

From the updated atomic models, integrated intensity histograms for all atoms were plotted for each of the two atomic models in comparison. A double Gaussian function was fitted to the intensity histogram to identify obvious Fe atoms (integrated intensity smaller than the Fe atom peak), obvious Pt atoms (integrated intensity larger than Pt atom peak), and borderline atoms near the overlapping region of two Gaussians. We manually examined every borderline atom and its paired atom in the comparison model. If the paired common atom is classified as an obvious Fe or Pt atom, the atomic species of the borderline atom was re-classified to be consistent with its paired common atom.

After updating the chemical species for the atomic models in comparison, we refined the 3D atomic coordinates to minimize the error between the calculated and measured projections using the procedure described elsewhere[34]. During the refinement, we monitored both the total embedded-atom potentials and the root-mean-square deviation (RMSD) of the atomic coordinates between the atom pairs of the two models. For the RMSD calculation, appropriate affine transformations were applied to the atomic models to correct for remnant distortions. The iterative refinement process was terminated when a minimum RMSD was reached.

After finalizing the 3D coordinates, all the atomic species of unpaired atoms or paired atoms with different species in each model were refined again using steps i)-iv) described above. These atoms could be classified as Fe, Pt or non-atoms. To minimize misidentification, the atoms previously identified as obvious Pt atoms remained unaltered, and the atoms previously identified as obvious Fe atoms were

prohibited from being identified as Pt atoms. Using this refinement procedure, we obtained the final refinement results of the seven atomic models with 3D atomic coordinates and species (Supplementary Table 1).

Order parameter calculation and nuclei identification. The order parameters of the atomic sites in the final atomic models were calculated for all 16 possible ordered phases from the FePt fcc lattice (four $FePt_3$ $L1_2$, four Fe_3Pt $L1_2$, six FePt $L1_0$, a Pt-rich A1, and a Fe-rich A1 phase) using the method described elsewhere[34]. Every atom was assigned to one of the 16 phases based on its highest order parameter. The nuclei in each atomic model were identified with the following procedure. For every atomic site, a sphere was drawn with the selected atom as the centre and a radius of 3.87 Å (one FePt fcc unit cell length). All the atomic sites inside the sphere were identified, which have the same ordered phase as that of the centre atom. If the highest order parameter atom inside the sphere is the centre atom, then the atom was defined as a core atom of a nucleus. Otherwise, the centre atom was tagged to be in the same nucleus as the highest order parameter atom, and a new sphere with the same radius and the highest order parameter atom as the centre was drawn to repeat the procedure until a nucleus core site was found. Applying this procedure to all atoms in each atomic model resulted in clusters of atoms with each cluster having a core. A cluster with a minimum of 13 atoms and order parameter ≥ 0.3 was defined as a nucleus in this study.

Identification of common nuclei. The nucleation dynamics study was performed on particles 2 and 3, which have three and two annealing times, respectively. To identify the common nuclei for particles 2 and 3 at different annealing times, we used the following criteria: i) Every common nucleus must have more than 50% overlap with at least one nucleus at different annealing times; ii) A common nucleus should have less than 50% overlap with any uncommon nuclei at different annealing times. Based on these two criteria, we found 33 common nuclei for particle 2, including 14 growing, 5 dissolving and 14 fluctuating nuclei. For particle 3, we found 25 common nuclei with 16 growing and 9 dissolving one. Since particle 3 has only two annealing times, it cannot be used to identify fluctuating nuclei.

Derivation of the OPG nucleation model. In the OPG model, each atom or molecule in a nucleus is assigned with an order parameter (α) between 0 and 1. By summing up the order parameter for all the atoms, the 1st term in equation (1) represent the effective volume energy difference of the nucleus. For example, for an atom with $\alpha = 0.6$, its contribution to the effective volume energy difference is *-0.6Δg *ΔV*, where *ΔV* is the volume occupied by the atom. To derive the 2nd term in equation (1), we divide a nucleus into many very small volumes (Supplementary Fig. 6e). The direction of the OPG inside each volume is along the Δs direction and the magnitude of the OPG is $\frac{|\Delta\alpha|}{\Delta d}$, where $\Delta\alpha$ is the order parameter difference in the volume and Δd is the distance along the OPG direction. The interfacial tension of this volume is calculated by

$$\frac{|\Delta\alpha|/_{\Delta d}}{1/_{\Delta d}} \gamma = |\Delta\alpha|\, \gamma \qquad (5)$$

where γ is the interfacial tension of a sharp interface with $\Delta\alpha = 1$. The total interfacial energy of the nucleus is obtained by adding up the interfacial energy of all the small volumes in the nucleus

$$\int|\Delta\alpha|\,\gamma\,ds = \gamma \int \left|\frac{\Delta\alpha}{\Delta d}\right|\, dV = \gamma \int |\vec{\nabla}\alpha|\, dV\,, \qquad (6)$$

which is the 2nd term in equation (1).

Next, we want to make a distinction between the OPG model and the square-gradient approximation[1,55]. The square-gradient approximation consists a square-gradient term, $\left(\vec{\nabla}\rho\right)^2$, where ρ is the density. There are three differences between the square-gradient and the magnitude-gradient term, $\left|\vec{\nabla}\alpha\right|$, in the OPG model.

First, the physical origin of the two terms is different. The square-gradient term is derived from the Taylor expansion of the density, as the integral of the gradient of the density is zero by summing it up along all the directions[55]. But the magnitude-gradient term is obtained by i) dividing a nucleus into many small volumes (Supplementary Fig. 6e); ii) normalizing the interfacial tension of each small volume with that of a sharp interface (equation (5)); and iii) integrating the interfacial energy of all the small volumes in the nucleus. Thus, the magnitude-gradient term has a lower order than the square-gradient one and the volume integral of the magnitude-gradient term (the 2nd term in equation (1)) has a physical meaning of the effective surface area of the nucleus.

Second, the coefficients of the two terms are different. The coefficient of the square-gradient term requires a complicated integration and is difficult to obtain[1,55]. On the other hand, the coefficient of the magnitude-gradient term is γ, which is the interfacial tension of a sharp interface between $\alpha = 1$ and 0. Furthermore, anisotropic γ can in principle be incorporated into the OPG model.

Third, the square-gradient approximation is part of the density functional theory[1,25,26,55], which represents the free energy change in terms of the density. The OPG model generalizes CNT by expressing the free energy change in terms of different types of order parameters and is applicable to both homogeneous and heterogeneous nucleation. For example, in this work we implemented two different types of order parameters in the OPG model to represent the chemical order/disorder transition of FePt (Figs. 3, 4, and Supplementary Figs. 4-7) and the liquid-solid phase transition of Pt (Fig. 5 and Supplementary Figs. 8 and 9). By using different order parameters, the OPG model can in principle be applied to other types of nucleation processes.

Implications of the OPG model. To provide a better understanding of the OPG model, we applied equation (1) to three special cases.

Case 1: A linear decrease of α (Supplementary Fig. 6f). We consider a spherical nucleus with a radius r and the order parameter specified by

$$\alpha = \alpha_0 \left(1 - \frac{r'}{r}\right). \qquad (7)$$

Substituting equation (7) into equation (1), we get

$$\Delta G = -\frac{\pi \Delta g \alpha_0 r^3}{3} + \frac{4\pi \gamma \alpha_0 r^2}{3} \ . \qquad (8)$$

By taking the derivative of ΔG with respect of r, we obtain the critical radius and the homogeneous free energy barrier,

$$r_c^* = \frac{2.67\gamma}{\Delta g} \qquad\qquad \Delta G^* = \frac{3.16\pi\alpha_0\gamma^3}{\Delta g^2} \ . \qquad (9)$$

For the heterogeneous free energy barrier, we have to multiply ΔG^* by a shape factor.

Case 2: A parabolic decrease of α (above the linear line in Supplementary Fig. 6f). The order parameter is represented by,

$$\alpha = \alpha_0 - \alpha_0 \left(\frac{r^{'}}{r}\right)^2 . \quad (10)$$

Substituting equation (10) into equation (1), we have the critical radius and the homogeneous free energy barrier,

$$r_c^* = \frac{2.5\gamma}{\Delta g} \qquad \Delta G^* = \frac{4.17\pi\alpha_0\gamma^3}{\Delta g^2} . \quad (11)$$

Case 3: A parabolic decrease of α (below the linear line in Supplementary Fig. 6f). The order parameter is specified by,

$$\alpha = \alpha_0 \left(\frac{r^{'}}{r} - 1\right)^2 . \quad (12)$$

From equations (12) and (1), we obtain,

$$r_c^* = \frac{3.33\gamma}{\Delta g} \qquad \Delta G^* = \frac{2.47\pi\alpha_0\gamma^3}{\Delta g^2} . \quad (13)$$

For a comparison purpose, the critical radius and the free energy barrier of homogeneous nucleation in CNT are

$$r_c^* = \frac{2\gamma}{\Delta g} \qquad \Delta G^* = \frac{5.33\pi\gamma^3}{\Delta g^2} . \quad (14)$$

As $\alpha_0 \leq 1$, for the three special cases the free energy barrier of the OPG model is lower than that of CNT. Furthermore, since case 3 deviates the most from CNT, its free energy barrier is the smallest among the three cases.

Next, we prove that for a monotonically decreasing order parameter distribution, $\alpha(r)$, the OPG model has lower free energy barriers than CNT for both homogeneous and heterogeneous nucleation. Mathematically, it is equivalently to show that, if the volume energy difference term remains the same for the OPG model and CNT,

$$\int \alpha(r)dV = \frac{4\pi}{3}R^3, \quad (15)$$

then the interfacial energy term of OPG is always lower than or equal to that of CNT,

$$\int |\nabla\alpha| \, dV \leq 4\pi R^2. \quad (16)$$

As $\alpha(r)$ monotonically decreases as the radial distance, we have $|\nabla\alpha| = -\alpha'$. Substituting this relation and equation (15) into equation (16), we can re-write equation (16) as,

$$\left(\int_0^\infty (-\alpha') \, r^2 dr\right)^{3/2} \leq 3 \int_0^\infty \alpha(r) \, r^2 dr. \quad (17)$$

Using Jensen's inequality[56] and integral by parts, we have,

$$\left(\int_0^\infty (-\alpha') \, r^2 dr\right)^{3/2} \leq \int_0^\infty (-\alpha')(r^2)^{3/2} \, dr = 3 \int_0^\infty \alpha(r) \, r^2 dr . \quad (18)$$

The derivation is for homogeneous nucleation. For heterogeneous nucleation we multiply the total free energy change by a shape factor and the remaining derivation is the same. Thus, we prove that for monotonically decreasing $\alpha(r)$, the OPG model is energetically more favourable than CNT.

MD simulations of heterogeneous and homogeneous nucleation in the liquid-solid phase transition of Pt. To further validate the OPG model, we performed MD simulations on two Pt nanoparticles and a Pt

bulk system using the LAMMPS package[46]. We first used an embedded-atom method potential to simulate a Pt nanoparticle of 32,000 atoms[47], which was put in a much larger box so that it does not interact with its periodic images. The nanoparticle was melt and equilibrated at 2,500 K and then quenched to room temperature with a cooling rate of 1 K·ps^{-1}. The heterogeneous crystal nucleation initiates at 1,050 K in the supercooling region. The potential energy significantly drops when crystallization initiates. To examine the detailed nucleation processes, we selected the cooling snapshot at 1,100 K and performed fixed temperature simulations at the 1,100 K using the NVT ensemble (constant number of particle, constant volume and constant temperature). Since the system was in supercooling region, the crystallization started at ~150 ps and ended at ~300 ps.

To cross-validate the MD results, we simulated another Pt nanoparticle of 13,500 atoms in the canonical (NVT) ensemble in LAMMPS using the interface force field as the interatomic potential[48]. The nanoparticle was melt at 2,750 K for 300 and the temperature was lowered to 2,000 K for 200 ps. At this temperature the Pt nanodroplet showed no nucleation. The nanodroplet was then quenched to 1,650 K for 1 ns with a cooling rate of 1.65 K·ps^{-1}. During this cooling period, nucleation and liquid-solid phase transitions of Pt were induced and observed. Coordinates were recorded every 1 ps during this part of the simulation and used to analyse the in-situ change of the order parameter and atomic displacements during the nucleation process.

In addition to heterogeneous nucleation, we also performed MD simulations of homogeneous nucleation using a bulk Pt system. An embedded-atom method potential was used to simulate 32,000 Pt atoms[47] and periodic boundary conditions were applied along three directions to eliminate the surface effects. The system was equilibrated at 2,500 K and quenched to room temperature with a cooling rate of 1 K·ps^{-1}. In contrast to the Pt nanodroplet, the bulk system crystallized at ~750 K during quench process, which is lower in temperature than the heterogeneous nucleation process. This is because the homogeneous system has much less nucleation sites than the nanodroplet. The nucleation process was examined at a fixed temperature of 800 K using the NPT ensemble (constant number of particle, constant pressure and constant temperature). The crystallization initiated in the first few picoseconds and ended at ~200 picoseconds.

Order parameter definition and nuclei identification for the MD simulation results. The order parameters of the Pt atoms in the MD simulations were calculated using local bond-orientation order parameter method[49,57,58]. The Q_4 and Q_6 order parameters were calculated up to the second shell with the shell radius of 3.8 Å as described elsewhere[58]. The order parameter was normalized between 0 and 1 where 0 corresponds to $Q_4=Q_6=0$ and 1 represents a perfect Pt fcc structure. To identify the nuclei formed during the heterogeneous and homogeneous nucleation, we applied the same method described above with a 4-Å-radius sphere and a minimum of 31 atoms. Common nuclei at different time points were also identified using the same method described above. Note that the local bond-orientation order parameter has been previously used to study crystallization with computer simulations[18,19].

51. Xu, C. *et al.* FePt Nanoparticles as an Fe Reservoir for Controlled Fe Release and Tumor Inhibition. *J. Am. Chem. Soc.* **131,** 15346–15351 (2009).

52. Lewis, J. P. Fast Normalized Cross-Correlation. *Vis. Interface* **95,** 120–123 (1995).

53. Dabov, K., Foi, A., Katkovnik, V. & Egiazarian, K. Image Denoising by Sparse 3-D Transform-Domain Collaborative Filtering. *IEEE Trans. Image Process.* **16,** 2080–2095 (2007).

54. Rogers, S. S., Waigh, T. A., Zhao, X. & Lu, J. R. Precise particle tracking against a complicated background: polynomial fitting with Gaussian weight. *Phys. Biol.* **4,** 220–227 (2007).

55. Cahn, J. W. & Hilliard, J. E. Free Energy of a Nonuniform System. I. Interfacial Free Energy. *J. Chem. Phys.* **28,** 258–267 (1958).

56. Krantz, S. G. Jensen's Inequality. in *Handbook of Complex Variables* (Boston, MA: Birkhäuser, 1999).

57. Steinhardt, P. J., Nelson, D. R. & Ronchetti, M. Bond-orientational order in liquids and glasses. *Phys. Rev. B* **28,** 784–805 (1983).

58. Wang, Y., Teitel, S. & Dellago, C. Melting of icosahedral gold nanoclusters from molecular dynamics simulations. *J. Chem. Phys.* **122,** 214722 (2005).
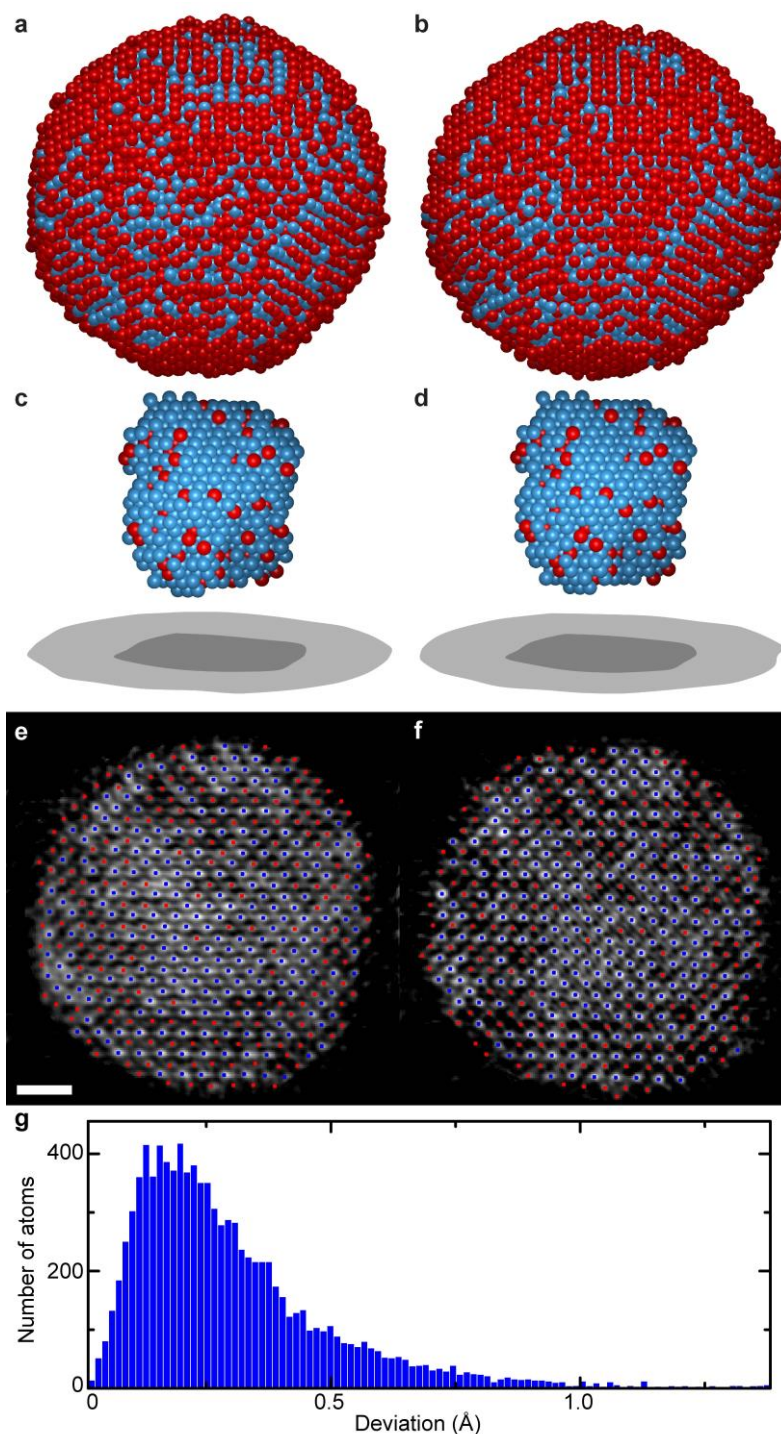
Supplementary Figure 1 | Consistency check of the AET measurements. a and **b**, 3D atomic models (Pt in blue and Fe in red) of particle 1 after 9 minutes of annealing at 520°C, determined by AET from two independent tilt series acquired under the same experimental conditions. **c** and **d,** Pt-rich cores cropped from the 3D atomic models shown in (**a**) and (**b**), respectively. **e** and **f**, The same atomic layer of the nanoparticle along the [010] direction (Pt in blue and Fe in red), obtained from the two independent measurements. Scale bar, 1nm. **g**, Histogram of the deviation of the common atoms between the two independent measurements, indicating 95.4% of the atoms are consistent. The average deviation between the two independent measurements is 37 pm. According to the statistical analysis of error propagation, the precision of the AET measurement is 37 pm $/\sqrt{2}$ = 26 pm.
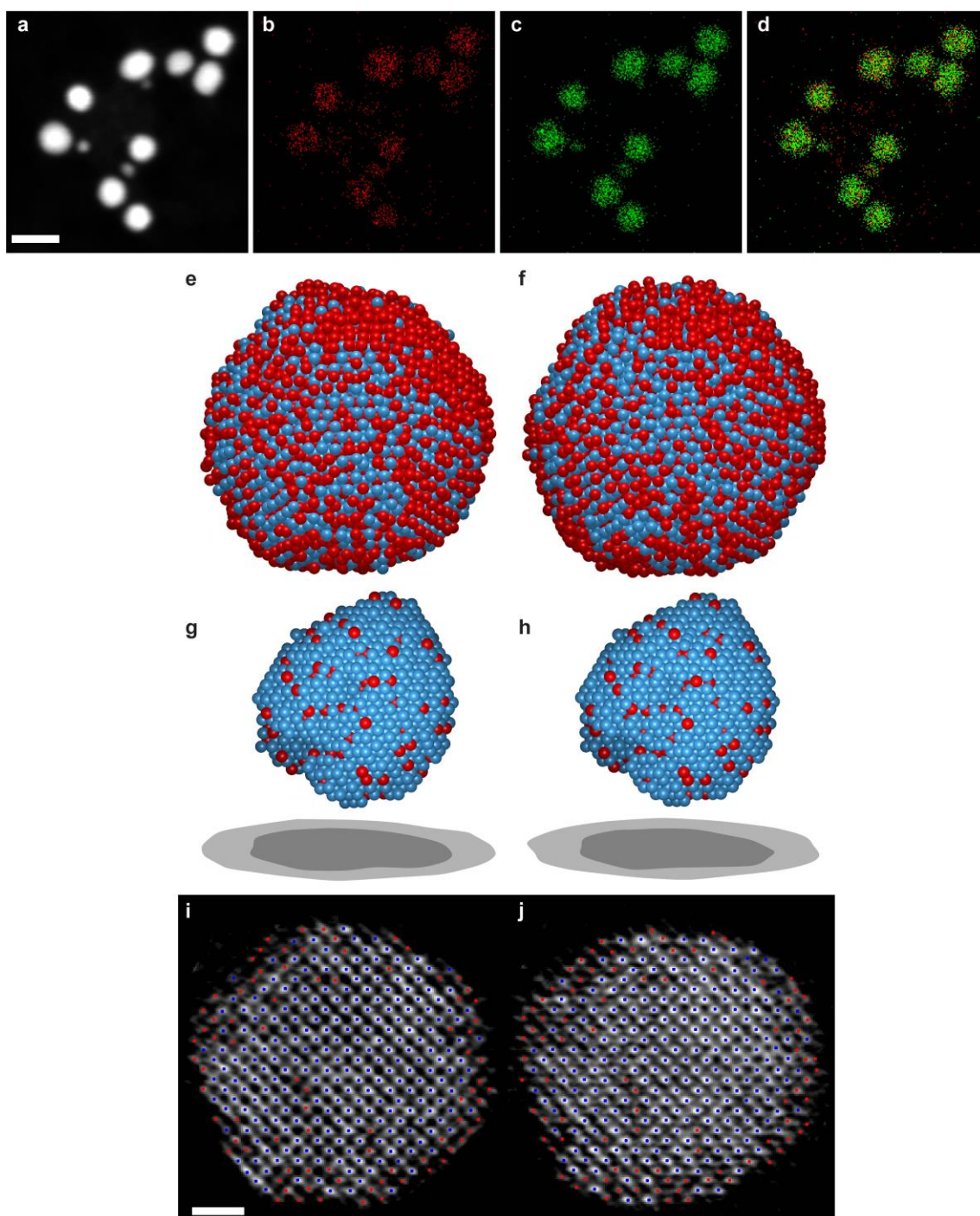
Supplementary Figure 2 | Distribution of Fe and Pt nanoclusters between FePt nanoparticles and two-time measurements of an FePt nanoparticle. a, ADF-STEM image of the FePt nanoparticles on a Si_3N_4 substrate. Energy-dispersive x-ray spectroscopy (EDS) images show the distribution of Fe (**b**), Pt (**c**), and both Fe and Pt nanoclusters (**d**) between FePt nanoparticles, acquired simultaneously with the ADF-STEM image (**a**). Scale bar, 10 nm. **e** and **f,** 3D atomic models (Pt in blue and Fe in red) of particle 3 with a total annealing time of 9 and 16 minutes, respectively, determined by AET. **g** and **h,** The Pt-rich core of the nanoparticle remained the same between the two annealing times. The light and dark grey projections show the whole nanoparticle and the core, respectively. **i** and **j,** The same atomic layer of the nanoparticle along the [010] direction at the two annealing times (Pt in and Fe in red), where a fraction of the surface and sub-surface atoms were re-arranged due to the annealing process, but the Pt-rich core of the nanoparticle did not change. Scale bar, 1nm.
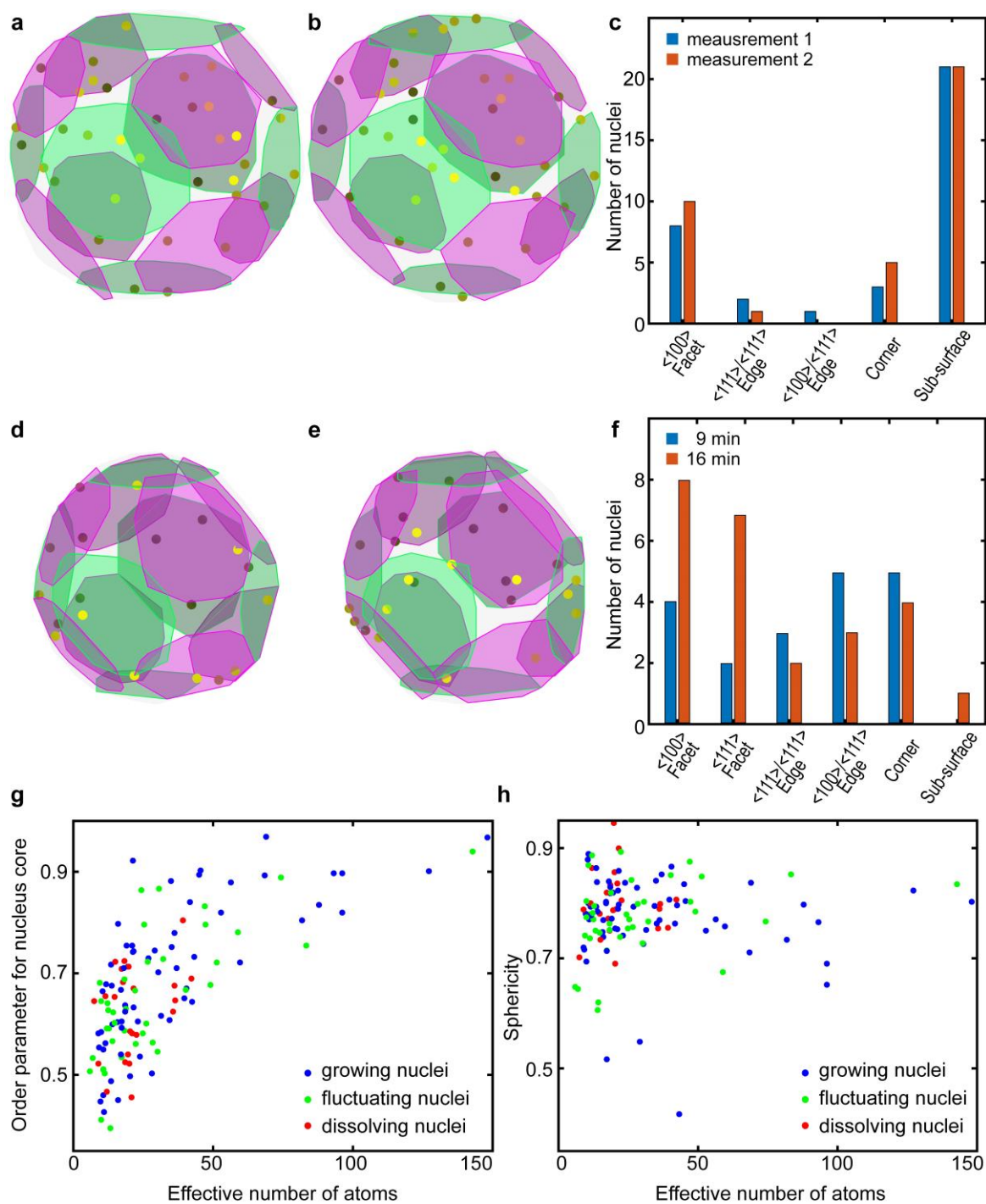
Supplementary Figure 3 | Analysis of the sites, cores and 3D shapes of early stage nuclei.
**a** and **b**, The distribution of the nucleation sites (circular dots) in particle 1, where the lighter colour dots are closer to the front side and the darker dots are closer to the back side of the nanoparticle. The <100> and <111> facets are in magenta and green, respectively. **c**, Histogram of the nucleation site distribution in particle 1. **d** and **e**, The distribution of the nucleation sites (circular dots) in particle 3 with an annealing time of 9 and 16 minutes, respectively. **f**, Histogram of the nucleation site distribution in particle 3. **g**, The order parameter of the nuclei core as a function of the effective number of atoms for particles 2 and 3. **h**, The sphericity of the nuclei as a function of the effective number of atoms for particles 2 and 3.
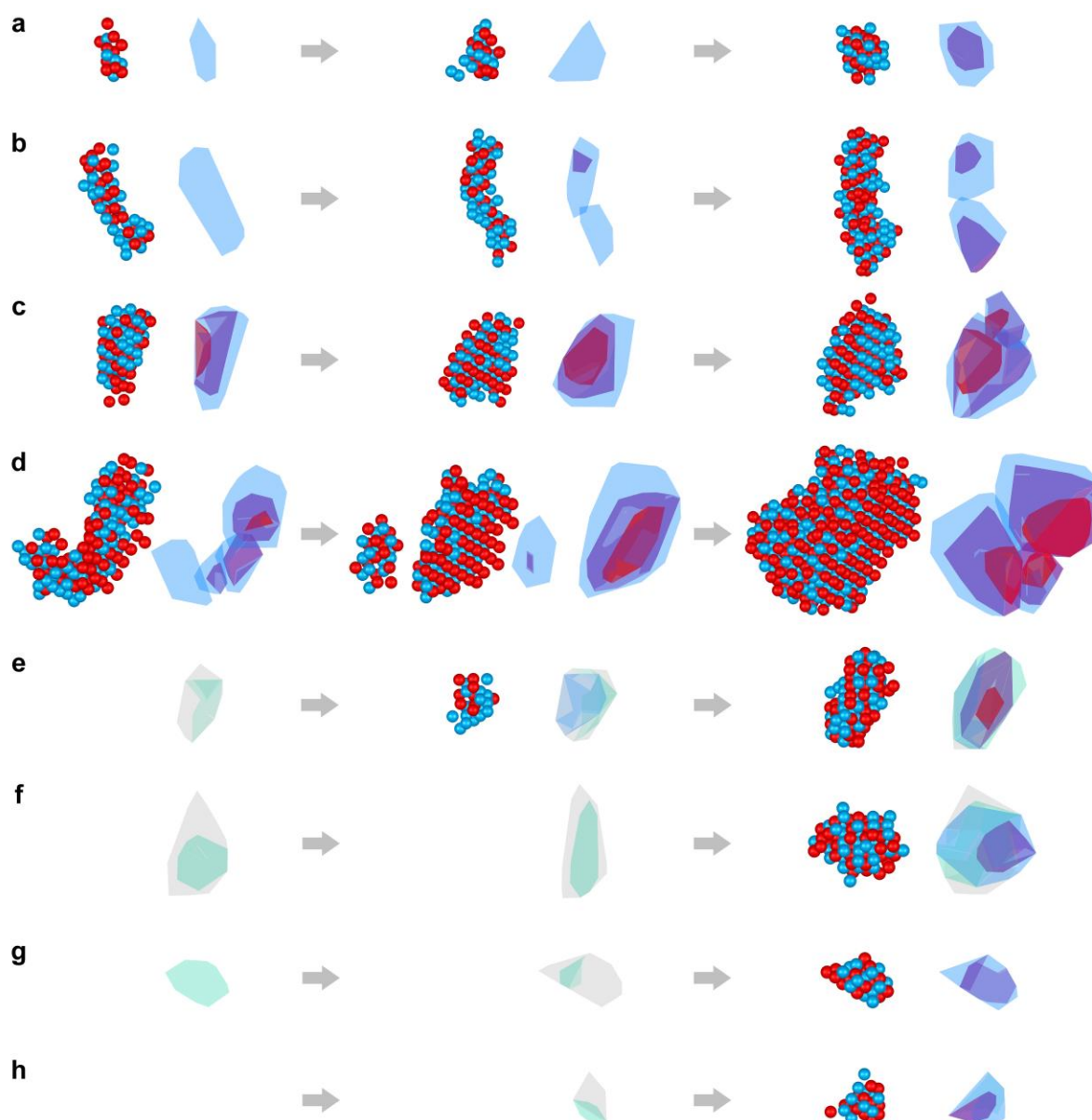
Supplementary Figure 4 | Experimental observation of growing nuclei at 4D atomic resolution. a-d, Four representative growing nuclei in particle 2 with a total annealing time of 9, 16 and 26 minutes, respectively, where the atomic models show Fe (red) and Pt atoms (blue) with an order parameter ≥ 0.3 and the 3D contour maps show the distribution of an order parameter of 0.7 (red), 0.5 (purple) and 0.3 (light blue). Dividing and merging nuclei are observed in (**b-d**). **e-h,** Another four representative growing nuclei in particle 2 with a total annealing time of 9, 16 and 26 minutes, where the 3D contour maps show the distribution of an order parameter of 0.7 (red), 0.5 (purple), 0.3 (light blue), 0.2 (green), and 0.1 (gray). No atomic model is displayed if a corresponding common nucleus was not identified at a specific annealing time. Another five growing nuclei in particle 3 similar to (**e-h**) are not shown here.
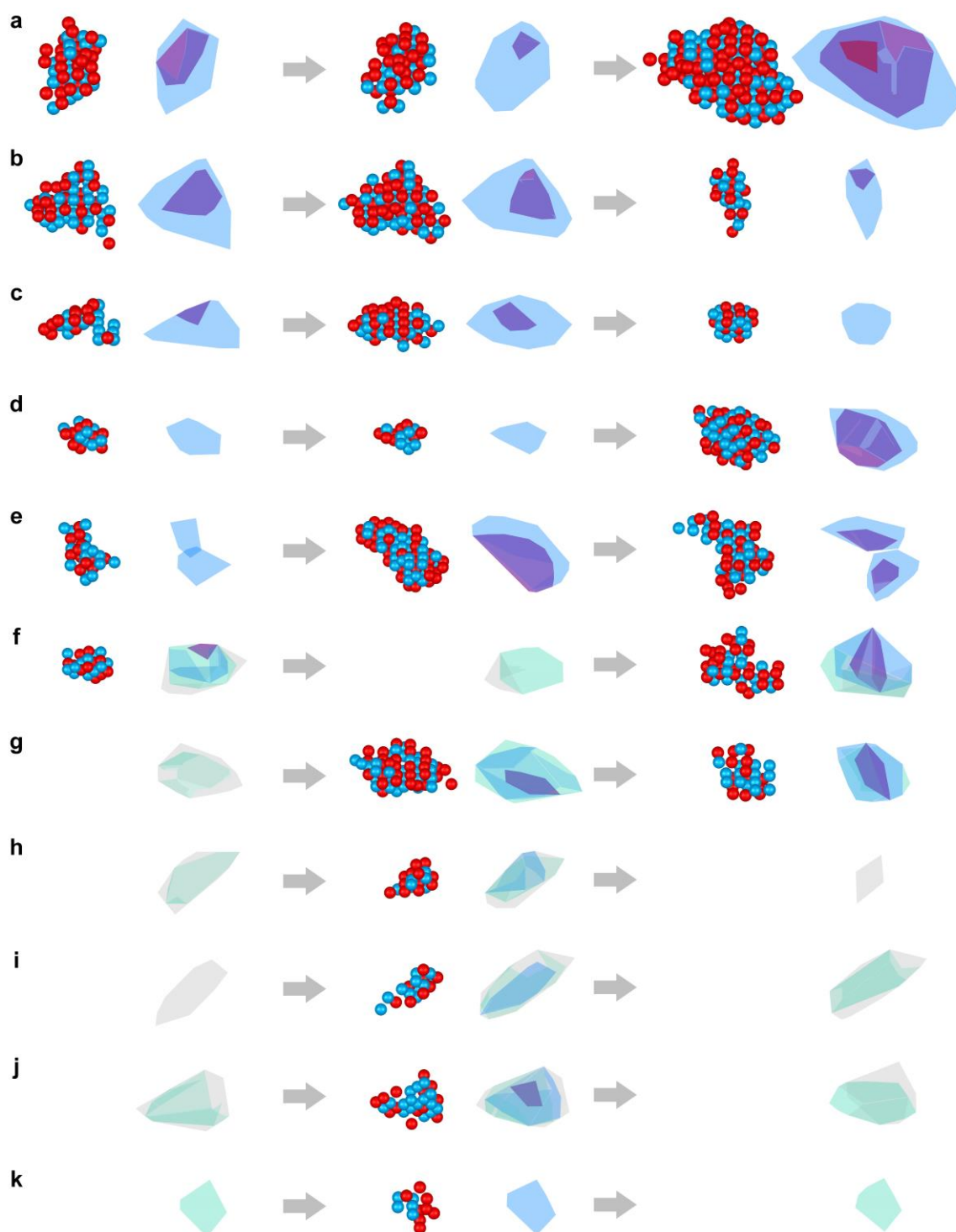
Supplementary Figure 5 | Experimental observation of fluctuating nuclei at 4D atomic resolution. a-e, Five representative fluctuating nuclei in particle 2 with a total annealing time of 9, 16 and 26 minutes, respectively, where the atomic models show Fe (red) and Pt atoms (blue) with an order parameter ≥ 0.3 and the 3D contour maps show the distribution of an order parameter of 0.7 (red), 0.5 (purple) and 0.3 (blue). Merging and dividing nuclei are observed in (**e**). **f-k**, Another six representative fluctuating nuclei in particle 2 with a total annealing time of 9, 16 and 26 minutes, where the 3D contour maps show the distribution of an order parameter of 0.7 (red), 0.5 (purple), 0.3 (light blue), 0.2 (green), and 0.1 (gray). No atomic model is displayed if a corresponding common nucleus was not identified at a specific annealing time.
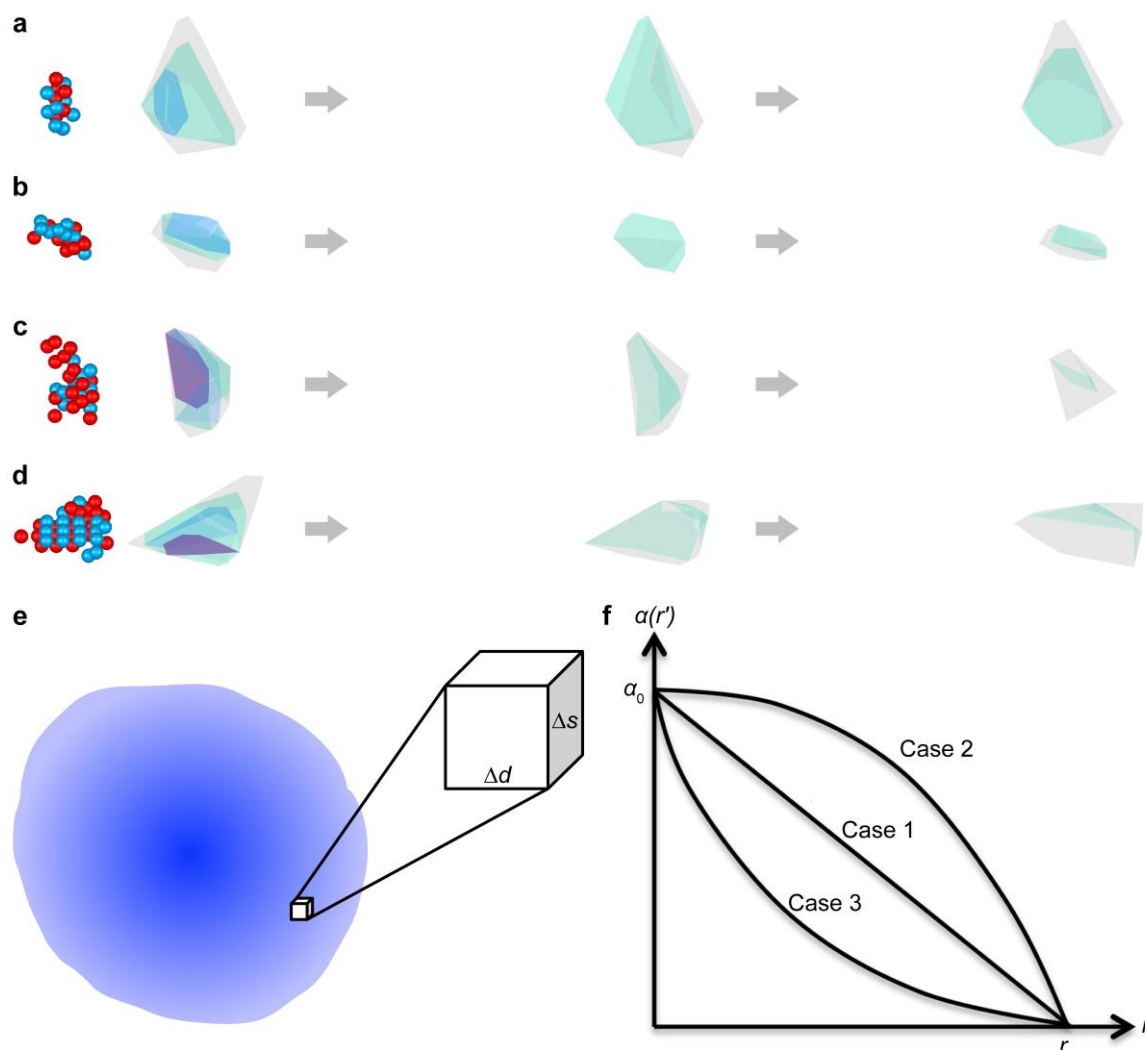
Supplementary Figure 6 | Experimental observation of dissolving nuclei and schematic illustrations for the OPG nucleation model. a-d, Four dissolving nuclei in particle 2 with a total annealing time of 9, 16 and 26 minutes, where the 3D contour maps show the distribution of an order parameter of 0.7 (red), 0.5 (purple), 0.3 (light blue), 0.2 (green), and 0.1 (gray). No atomic model is displayed if a corresponding common nucleus was not identified at a specific annealing time. **e,** Schematic illustration of a nucleus with varying order parameters. The nucleus is divided into many very small volumes for the calculation of the interfacial energy. **f,** Three specific cases with the other parameter, $\alpha(r)$, linearly or parabolically decreasing as the radial distance.
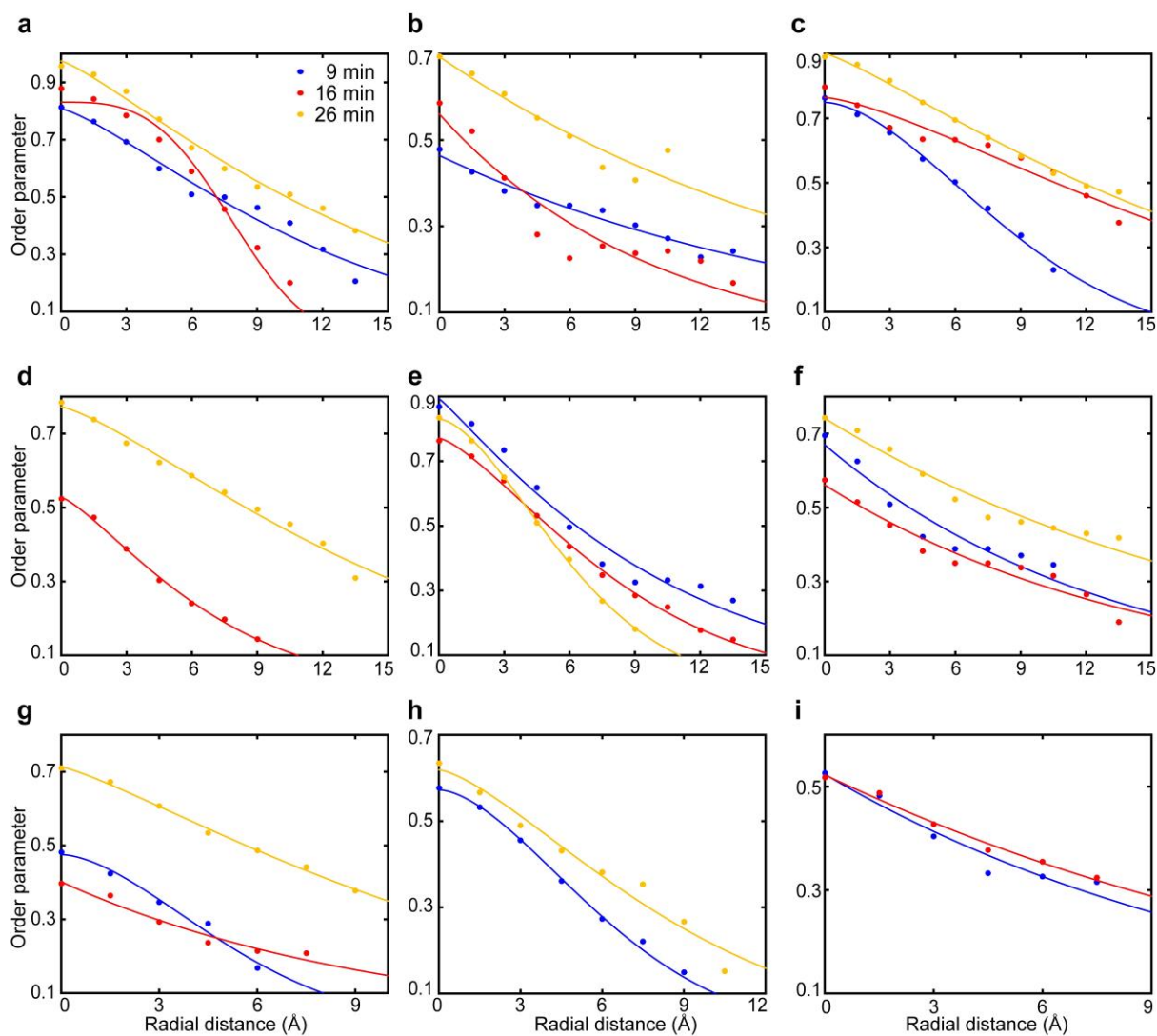
Supplementary Figure 7 | Radial average order parameter distributions of nine representative nuclei. The order parameter distributions for four growing nuclei (**a-d**), four fluctuating nuclei (**e-h**) and one dissolving nucleus (**i**) in particle 2, where the dots represent the experimentally measured data and the curves are fitted with equation (4).
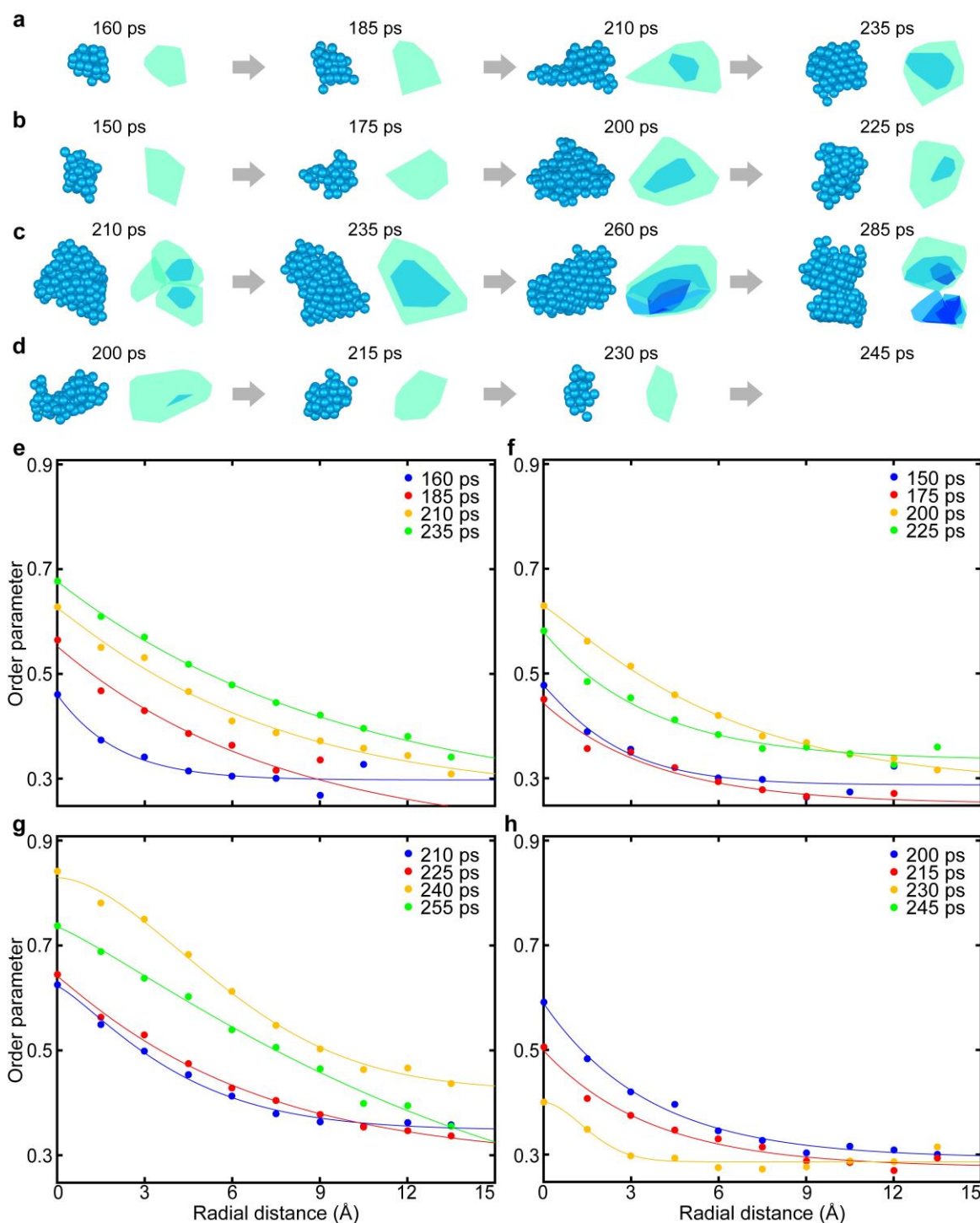
Supplementary Figure 8 | Nucleation dynamics in the liquid-solid transition of a Pt nanoparticle, obtained by MD simulations with the interface force field. **a**, A representative growing nucleus, where the atomic models show the Pt atoms with an order parameter ≥ 0.3 and the 3D contour maps show the distribution of an order parameter of 0.7 (dark blue), 0.5 (light blue) and 0.3 (cyan). **b** and **c**, Two representative fluctuating nuclei, where merging and dividing nuclei are observed in (**c**). **d**, A representative dissolving nucleus, which dissolved at 245 ps. **e-h**, Radial average order parameter distributions of the four nuclei shown in (**a-d**), respectively, where the dots were obtained by time-averaging ten consecutive MD snapshots with 1 ps time intervals and the curves are the fitted results using equation (4) with a constant background.
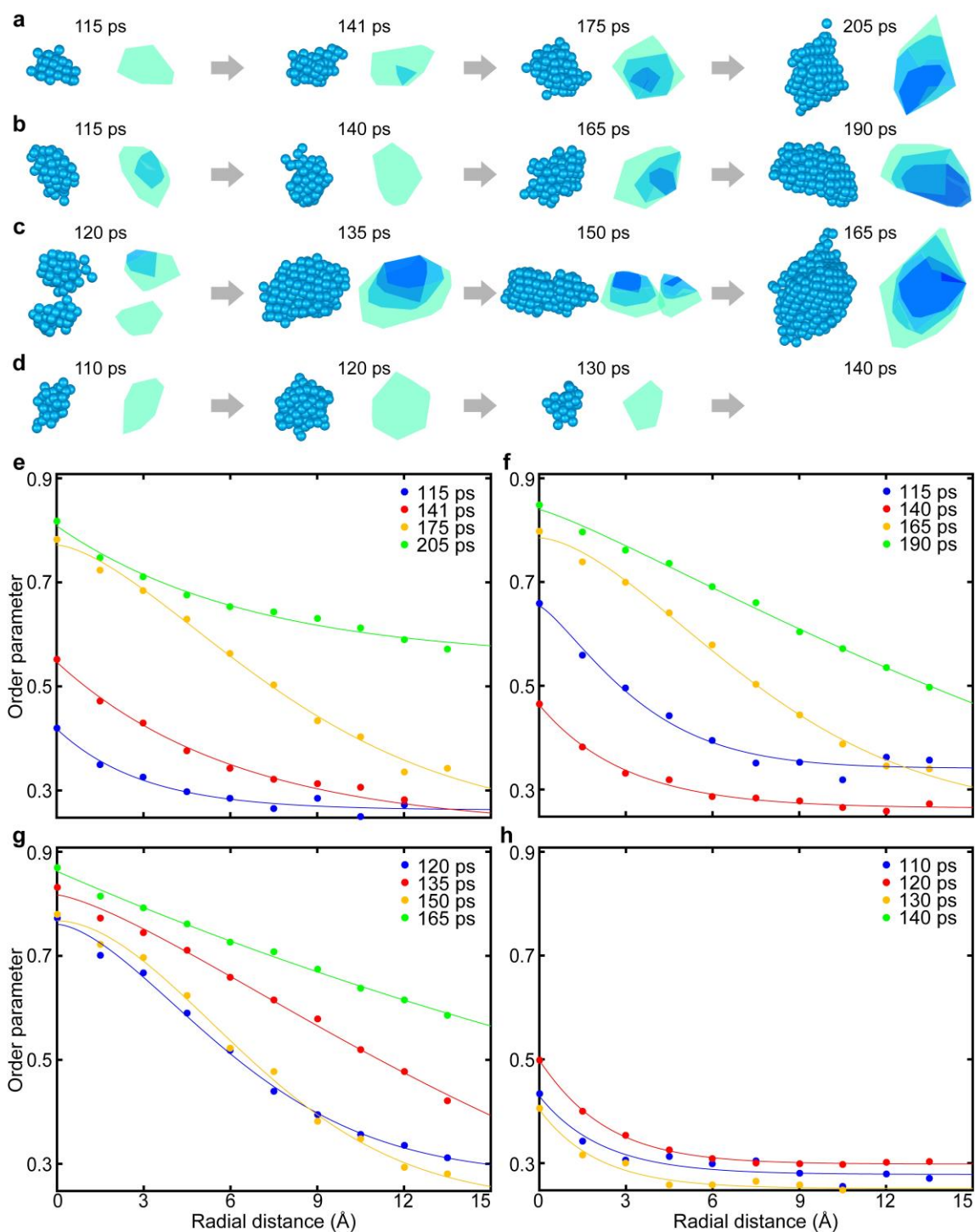
Supplementary Figure 9 | Nucleation dynamics in the liquid-solid transition of a bulk Pt system, obtained by MD simulations with the embedded-atom method potential. **a**, A representative growing nucleus, where the atomic models show the Pt atoms with an order parameter ≥ 0.3 and the 3D contour maps show the distribution of an order parameter of 0.7 (dark blue), 0.5 (light blue) and 0.3 (cyan). **b** and **c**, Two representative fluctuating nuclei, where merging and dividing nuclei are observed in (**c**). **d**, A representative dissolving nucleus, which dissolved at 140 ps. **e-h**, Radial average order parameter distributions of the four nuclei shown in (**a-d**), respectively, where the dots were obtained by time-averaging ten consecutive MD snapshots with 1 ps time intervals and the curves are the fitted results using equation (4) with a constant background.

Supplementary Table 1 | AET data collection, reconstruction, refinement and validation statistics

	Particle 1		Particle 2			Particle 3	
	Tilt series #1	Tilt series #2	Tilt series #3	Tilt series #4	Tilt series #5	Tilt series #6	Tilt series #7
Data collection and processing							
Annealing time (min)	9	9	9	16	26	9	16
Voltage (kV)	200	200	200	200	200	200	200
Convergence semi-angle(mrad)	30	30	30	30	30	30	30
Probe size (Å)	0.7	0.7	0.7	0.7	0.7	0.7	0.7
Detector inner angle (mrad)	38	38	38	38	38	38	38
Detector outer angle (mrad)	190	190	190	190	190	190	190
Depth of focus (nm)	6	6	6	6	6	6	6
Pixel size (Å)	0.34	0.34	0.34	0.34	0.34	0.34	0.34
# of projections	57	55	52	52	51	52	52
Tilt range (°)	−64.3 +65.3	−64.3 +65.5	−62.3 +63.1	−62.3 +63.0	−62.0 +62.1	−62.3 +63.1	−62.3 +63.0
Electron dose (10^5 e/Å^2)	8.5	8.2	7.7	7.7	7.6	7.7	7.7
Reconstruction							
Algorithm	GENFIRE	GENFIRE	GENFIRE	GENFIRE	GENFIRE	GENFIRE	GENFIRE
Interpolation method[a]	DFT	DFT	DFT	DFT	DFT	DFT	DFT
Interpolation radius (voxel)	0.1	0.1	0.1	0.1	0.1	0.1	0.1
Oversampling ratio	4	4	4	4	4	4	4
Refinement							
R_1 (%)[b]	7.8	7.8	12.9	10.5	8.8	8.7	9.2
R (%)[c]	20.8	20.0	14.7	17.0	17.9	15.8	15.4
B' factors (Å^2)							
Fe atoms	24.3	22.3	25.4	25.0	23.0	23.4	23.5
Pt atoms	35.2	25.5	26.8	34.7	27.6	25.6	28.1
# of atoms							
Fe	5356	5407	1640	1773	2291	2103	2313
Pt	5107	5066	3195	3295	3195	4078	4127
# of Common atoms							
Fe	4996	4996	1375	1375/1383	1383	1805	1805
Pt	4986	4986	3090	3090/2808	2808	3880	3880

[a]GENFIRE uses either the discrete Fourier transform or the fast Fourier transform to obtain the Fourier coefficients. The former is slower but more accurate than the latter. [b]The R_1-factor is defined as equation (5) in ref. 34. [c]The R-factor is defined as $R = \frac{\sum ||F_{obs}| - |F_{cal}||}{\sum |F_{obs}|}$, where $|F_{obs}|$ is the Fourier magnitude obtained from experimental data and $|F_{cal}|$ the Fourier magnitude calculated from an atomic model.